In-situ observations of marine aggregate using imaging systems

Doctoral Dissertation

IN-SITU OBSERVATIONS OF MARINE AGGREGATE USING IMAGING SYSTEMS

March 2020

Graduate School of Marine Science and Technology

Tokyo University of Marine Science and Technology

Doctoral Course of Applied Marine Environmental Studies

Marika Takeuchi

Doctoral Dissertation

IN-SITU OBSERVATIONS OF MARINE AGGREGATE USING IMAGING SYSTEMS

March 2020

Graduate School of Marine Science and Technology

Tokyo University of Marine Science and Technology

Doctoral Course of Applied Marine Environmental Studies

Marika Takeuchi

Abstract

Marine aggregates are formed through the coagulation of small biogenic and non-biogenic components. Visible aggregates, known as marine snow, are typically in the 0.5 mm to a few mm size range. Aggregates are well recognized as hotspots of microbial and planktonic activities. In addition, aggregates formation is an important pathway to transfer organic materials from the surface to the deep ocean; hence the impacts of aggregates in carbon flux is significant. Since carbon mass content, chlorophyll-*a* concentration, and aggregate sinking velocity are size dependent, aggregate size distribution is fundamental to better understand the contribution of aggregate in the marine ecosystems and future climate changes. Numerous studies have been conducted at laboratories and theoretical ways to demonstrate size distribution of aggregate through aggregation and destruction of cultured aggregate or idealized particles; however, the size distribution of naturally occurring aggregate has not fully investigated in field studies. In this study, I will present the relationships between size distribution of aggregate and i) turbulence and ii) chlorophyll-*a* using *in-situ* data. Furthermore, I will explore the seasonal variation of aggregate from a long-term monitoring system. Introducing a recommended way of aggregate measurements in the field will be presented in the end.

A mini CMOS camera (DSLII 190, Little Leonard Inc.) was mounted on a free-fall microstructure profiler (TurboMAP-L, JFE Advantech Co., Ltd.) and collected images of

aggregates simultaneously with turbulence parameters. Observations were conducted at 10 different locations since 2008. Images that Digital Still Logger (DSL) camera collected were subsequently used to determine aggregate size distributions.

Three physical mechanisms are known to form aggregate; Brownian motion, differential sedimentation and turbulence. Brownian motion is a main driver to form small aggregate through collisions of small particles (<1μm). The influence of differential sedimentation is relatively small under turbulent conditions. Thereby, turbulence is expected to be the major driver to form large aggregates in the upper ocean. In order to reveal the relationship between turbulence and aggregate sizes, turbulent kinetic energy dissipation rate (ε, W kg^{-1}) estimated from shear data and major axis length of aggregate (*MajAL*, cm) were directly compared. Each variable was averaged over 10 metres. Direct comparison of average turbulence kinetic energy dissipation rate ($\bar{\varepsilon}$, W kg^{-1}) and average *MajAL* ($\overline{MajAL}$,cm) showed a positive correlation in log-scale (r^2 = 0.52, n =567, p<<0.01), exhibiting that aggregates becomes larger when turbulent intensity increases. Majority of $\overline{MajAL}$ remained below the Kolmogorov scale (the smallest eddy size), suggesting that aggregate size is limited by the Kolmogorov scale. It also showed 90 % of $\overline{MajAL}$ was smaller than 0.1 cm which corresponds to the Kolmogorov scale at $\varepsilon = 10^{-6}$ W kg^{-1}. This demonstrates that turbulence below $\bar{\varepsilon}=10^{-6}$ W kg^{-1} enhances aggregation, increasing average particle size; greater turbulence causes particle breakup, limiting the average maximum aggregate

size. Since ε does not exceed 10^{-6} W kg^{-1} in most water column away from boundaries, turbulence has a significant influence on the formation of aggregate in the most of water column in the world ocean. $\overline{MajAL}$ was also compared with total concentration of aggregate (V_{agg}, ppm). V_{agg} indicates the fraction of water that is occupied with aggregate. Log_{10} ($\overline{MajAL}$) and $\log_{10}$ (V_{agg}) also showed a positive correlation (r^2 = 0.81, n =567, p<<0.01). The collision rate of aggregate increase when water is more occupied with aggregate, leading a formation of larger aggregate. Morphological change has also been investigated in this study. The comparison between average aspect ratio and $\bar{\varepsilon}$ showed a positive correlation, suggesting that aggregate becomes elongated under strong turbulence.

Doubell et al., (2009) suggested that number of aggregates in the images increased when laser fluorescence probe on TurboMAP-L showed locally strong signals. Since laser fluorescence probe resolves ~2mm scale, they hypothesized that such strong signals were obtained from hitting individual aggregates. Secondly, I present the relationship between aggregates and fluorescence signals. In order to compare the strong signals of laser fluorescence and aggregates, strong signals that exceeded a threshold (1.5 × 1 metre moving average) were integrated over 10 metres (*ILFI*, μg L^{-1} /10m). *ILFI* was then compared with total volume concentration of aggregates (V_{agg}, ppm). Smaller V_{agg} was found in the open water than the coastal water, showing that water is less occupied with aggregates in the open water. It also showed smaller V_{agg} in open water for given *ILFI*.

This suggests that individual aggregates in the open water contain more phytoplankton. Thereby phytoplankton is densely concentrated in the open water. The open water environments, such as the Kuroshio extensions, are known to be oligotrophic. Highly dense phytoplankton in induvial aggregate in the open water may be playing an important role as a source of nutrient and food for other living organisms in the oligotrophic environments.

The observations by DSL camera and TurboMAP-L show snapshot of aggregate distribution in water column, but do not provide time series data to investigate the seasonal variation. Long term monitoring of aggregates by a cabled observatory system (OCEANS) was conducted to explore the seasonal variation of aggregates. OCEANS was deployed at a coastal environment (~20 m from surface) near Habu port of Oshima island. Data were continuously collected since 2014. Two periods (October-January in 2015 and 2016) were selected to compare in this study. Strong influence of the open water from the Kuroshio was found in the 1st period and the 2nd period had a coastal water characteristic. The frequency of aggregate appearance was higher in the 1st period. During the 1st period, relatively larger aggregate with more transparent exopolymer particles (TEPs) was observed. Smaller aggregate with less TEPs was dominant during the 2nd period. Since other plankton abundance is also available, further investigation for the biological

interaction between aggregate and other organisms is required for better understanding of ecosystems.

Observation of naturally occurring aggregate was successfully conducted by DSL camera, TurboMAP-L, and OCEANS, since DSL camera mounted on TurboMAP-L allowed non-disruptive measuring of aggregate in a free fall mode and OCEANS was fixed at the seabed. At the end of this dissertation, a comparison between the size distribution of aggregates obtained by DSL camera and holographic camera systems are presented. Holographic cameras were lowered by a tethered cable mounted on a shipboard winch. Because of this, rocking motion of vessel caused sudden upward and downward motion of holographic cameras. The upward velocity of holographic cameras even reached 1 m s^{-1}. Size distribution clearly showed that aggregate was destroyed during the measurements by the flame of holographic cameras. Since holographic cameras are powerful tools to sample the water column with high resolution images, developing a new deployment method that allows non-disruptive measurements of aggregate, such as a free fall technology, is highly desirable.

Acknowledgements

I would like to express my deep gratitude to my supervisors Prof. Hidekatsu Yamazaki and Prof. Jim Mitchell who provided great support and guidance throughout my PhD works. Prof. Yamazaki has always been my best advisor since the start of my undergraduate education. He has provide great opportunities which definitely changed my life in many positive ways. There is no instrument that can accurately measure how much I appreciate his guidance. Prof. Mitchell has also given me wonderful opportunity to study in Adelaide. Chocolate supply from him was a big encouragement. The world tour was such an amazing experience. I also would like to express my appreciation to my co-supervisors Prof. Takeyoshi Nagai and Prof. Hisayuki Arakawa for their advices and warm encouragements. Many thanks to the co-authors of *Scientific Reports*, Prof. George Jackson, Dr. Mark Doubell, Mr. Yosuke Sagara and Ms. Misuzu Yukawa. The work was completed under very huge supports from all of these co-authors and there is never enough words to describe my appreciation to them. I am also thankful to Prof. Alex Nimmo Smith, Dr. George Graham, Prof. Hideki Fukuda, Prof. Rubens Lopes and Dr. Leandro Ticlia who kindly provided their data for holography and CPICS analysis. Many thanks to all my lab members in Tokyo and Adelaide, in particular, Prof. Eiji Masunaga, Dr. Hikaru Homma, Dr. Herminio Foloni and Dr. Mamoru Tanaka who supported me since my undergraduate project. Also, many thanks to Eri Nakamura, Miho Yatsunami, Mie Akada, Miwa Iwamura and Masako Iwasa who kept me smile everyday throughout my work since undergraduate. Many many thanks to Belinda Ng, my lovely roommate in Adelaide. She made my life in Adelaide wonderful. I also appreciate her encouragement.

Special thanks to my parents for supporting me in many ways for many years, my brothers Ray and Sho for always standing by me and keeping me smile and all my cats, Monica, Tipsy, Fefei, Ginger, Bebe and Shammy. Finally, a biggest thank you to Ashely Brereton who was always being the brightest lighthouse during this journey. Thank you very much for sailing together.

Table of Contents

List of figures

List of tables

List of equations

Chapter 1. Introduction

1.1. History of marine snow studies

Marine aggregates are widely distributed in aquatic systems. They are formed through particle collisions and large visible ones (>0.5 cm) is commonly known as “marine snow”, since the view of sinking aggregates looks like snowing under the water. The presence of aggregates has already been recognised in early 1930s when submarine systems enabled scientists to travel underwater world (Silver and Shanks 1978). Aggregates were not attracting much scientists’ attention when they were found; however, fishermen in Japan were aware of the links between presence of aggregates and fishing conditions (Tsujita 1953). The study of aggregates started in 1940s in Japan, as a possible predictor of local fishing condition. Samples collected from surface water showed that individual aggregate is consisting of phytoplankton and mucus particles that is now known as Transparent Exopolymer Particles (TEPs) (Figure1, Tsujita 1953). It was concluded that an aggregate was a community of dead organic materials at this time.

As scuba diving was introduced, aggregate studies have shown dramatic improvement because *in-situ* sampling became available. Aggregate is known to play many important roles in ecosystems. Experimental studies have shown that aggregate as a hotspot of nutrient and organisms (Azam and Long 2001; Stocker 2012). Rich chlorophyll-*a* and

bacteria was found in an individual aggregate (Alldredge and Gotschalk 1989), showing that aggregate is not a community of “dead” organisms but live organisms (Figure 1.2). Laboratory experiments have also shown that zooplankton and fish feed on aggregate (Kiøboe 2001; Larson and Shanks 1996). Furthermore, aggregate is recognised as an important carbon pathway to deeper water that may have a significant impact on climate changes, since sinking speed is higher than individual phytoplankton cells (Passow and Carlson 2012).

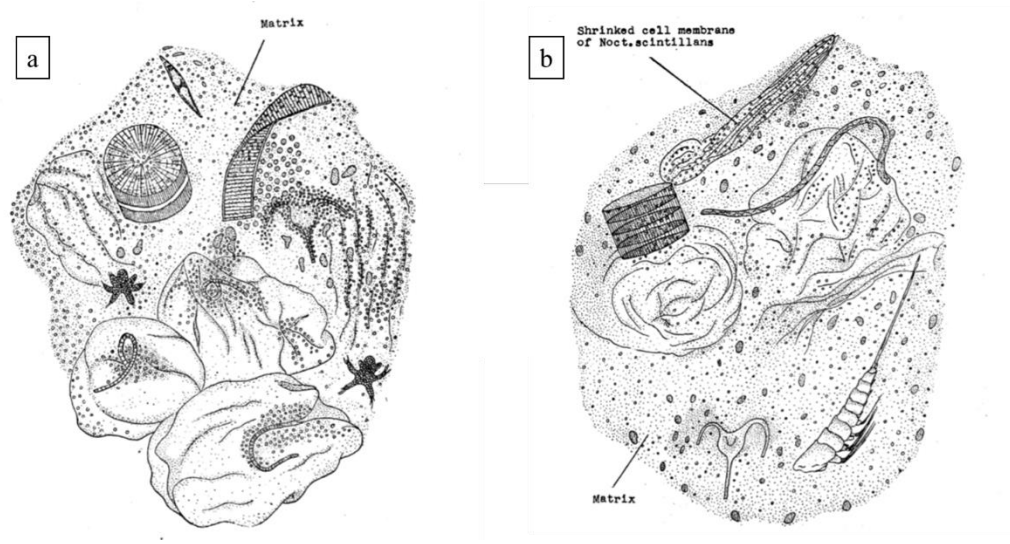

Figure 1.1Sketch of aggregate collected from near surface water (Tsujita 1953, Japan Oceanography Society). Many different organisms (diatoms, dinoflagellate, chaetognatha, copepod) were described at components of aggregate. Matrix is the mucus-rich cells, which is called TEPs.

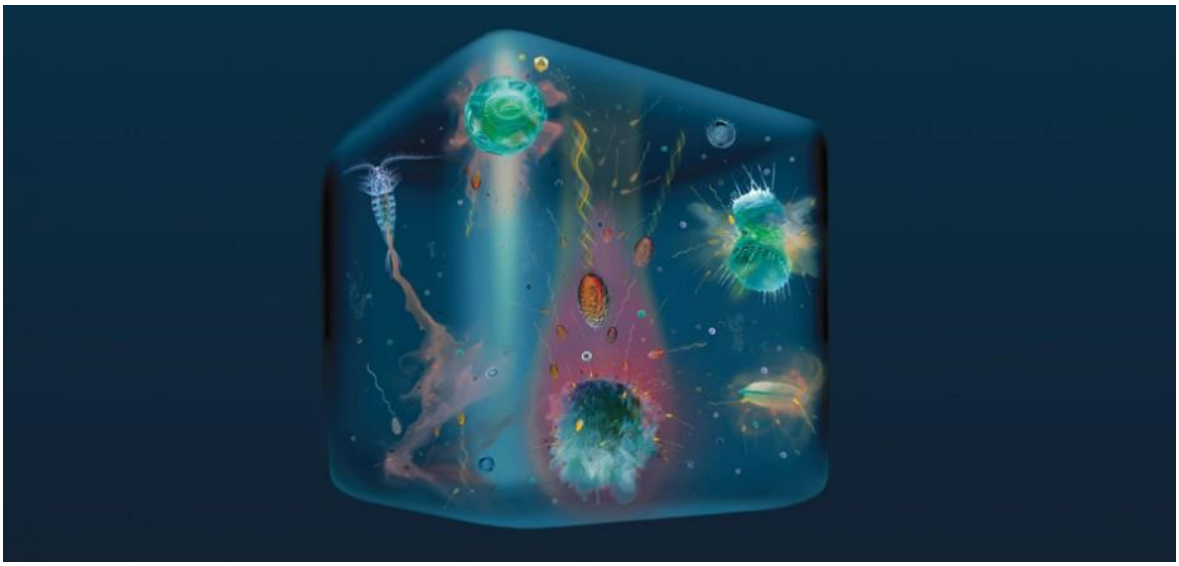

Figure 1.2 Conceptual view of aggregate in micro-scale ecosystem. Image was downloaded from the website of Stocker's lab; A Drop of Ocean (credit: Glynn Gorick, Justin Seymour and Roman Stocker; Science 2012).

1.2 Aggregate formation and destruction

Theoretical studies have shown that aggregate is formed through particle collision (Jackson 1990). Three physical mechanisms are known to drive particle collisions; Brownian motion, differential sedimentation and turbulence (Jackson 1990). Transparent Exopolymer Particles (TEPs) secreted from phytoplankton glue collided particles and form aggregate. Aggregate destruction (disaggregation) is caused by turbulent shear and differential sedimentation, self-erosion during sinking, and prey.

Among three physical mechanisms, turbulence has most significant impact on large aggregate (>1mm) (Burd and Jackson 1997). However, the roles of turbulence on

aggregate is still not clarified from field observational data due to limitation of *in-situ* measurement methods.

1.3 Observational methods

Formation and destruction processes of aggregates have been well studied in laboratory experiments and theoretical studies. However, the observational evidence is still limited because *in-situ* measurements of aggregate is technically challenging. Direct sampling of aggregate by a scuba diver was a major sampling method in 1990s. Unfortunately, this method limits the number of samples. Sampling water using Niskin bottles and direct collection by towing net certainly increase the volume of sample water. However, aggregate is always destroyed through bottle or net sampling due to the fragile nature of aggregates. Therefore, these sampling methods cause underestimation of aggregate size and overestimation of aggregate abundance.

Imaging systems such as Video Plankton Recorder (Gallager et al. 2004) or holographic systems (de Jong et al. 2010) can collect vast number of images of plankton including aggregate; however, mounting frames around the camera and profiling method (towing and winch controlled) may cause destruction of aggregates. Particle size represented by LISST systems (Sequoia Scientific Inc.) is also widely used for aggregate measurements in estuaries (Braithwaite et al. 2012; Mikkelsen et al. 2006). It does not likely cause aggregate

destruction, but LISST does not collect images of target particles. Therefore it is not clear that the measured particles are aggregates or not. Measured particles are most likely sediment flocs, since it is commonly used near the seabed. In addition, measurements are usually conducted at a bottom boundary layer that does not represent most water column in the open water. Developing a method that measures aggregate without destroying and vertical water column is required to further understand physical mechanisms of aggregate formation and destruction in the water column in the world ocean.

1.4 Layout of the dissertation

The objective of this study is to develop a series of techniques to understand natural features of marine aggregates using *in-situ* field data. Doubell et al. (2009) has developed a non-disruptive method of aggregate measurements. They mounted a Digital Still Logger (DSL) camera on a microstructure profiler (TurboMAP-L). Aggregates were successfully recorded by the DSL camera system without destruction throughout the water column, since TurboMAP-L was in a free-fall mode. In this study, a 5 years data set from 10 different csmpains is used. In Chapter 2, it is aimed to clarify the roles of turbulence on aggregate (aggregation and disaggregation) using aggregate images and turbulence data. In Chapter 3, microscale fluorescence data were compared with total volume concentration of aggregates. In Chapter 4, a long term observation of marine aggregates using a cabled

observatory is presented to investigate the seasonal change in aggregate properties. In Chapter 5, a potential risk of destroying aggregate during measurements using tethered instruments is presented. Holographic systems were lowered by a tethered cable attached to a shipboard winch and the images were compared with the images collected by a free fall system (TurboMAP-L) to investigate the difference in the outcomes. The conclusions of this study and future outlook are presented in Chapter 6.

Chapter 2. Turbulence and formation and destruction of aggregate

2.1 Introduction

Marine aggregates range in size from approximately 1 micrometres to several centimetres (Simon et al. 2002). Formed in the sunlit upper layers of the ocean and composed predominantly of organic material (Simon et al. 2002; Silver and Shanks 1978; Turner 2015), aggregates sink as a constant drizzle to the deep ocean (Turner 2015) and biogeochemical transformations along the way (Azam and Long 2001). Aggregate formation occurs through the collision and adhesion of smaller particles into larger particles and is driven by three main physical processes (McCave 1984; Jackson 1990). Brownian motion controls the collision of small particles (<1 μm). Differential sinking involves faster settling particles overtaking and colliding with slower settling particles and dominates for particle sizes between about 1 and 100 μm. Turbulent shear dominates the interactions between larger particles (McCave 1984) (>100 μm). Since large aggregates have increased sinking velocity and carbon content relative to small aggregates (Alldredge 1998), the mechanisms controlling aggregate size distribution in the upper ocean have important consequences for determining the transport of carbon to the deep ocean (Stemmann et al. 2004; Passow and Carlson 2012). The role of turbulence on aggregates has been investigated theoretically and experimentally (Guseva and Feudel 2017) over a range of flow conditions and materials,

usually using idealized shear models and uniform spheres as source particles (Soos et al. 2008). However, our understanding of the influence of turbulence on aggregates in the upper ocean interior has remained constrained due to a lack of direct observations. Early laboratory (Dyer and Manning 1999) and modelling (Ruiz and Izquierdo 1997) studies indicated that turbulence was important for both aggregation and disaggregation, consistent with the conceptual view of sedimentation processes in estuarine systems (Dyer and Manning 1999). Subsequent observations made in the sediment-rich benthic boundary layer revealed that our understanding of particle disaggregation remains uncertain (Hill, et al. 2001) with minimal influence of turbulence detected on aggregate size, even though modelling of disaggregation processes in the bottom boundary layer predicted aggregate breakup under strong turbulence (Ruiz and Izquierdo 1997).

In comparison to early experimental and modelling studies (Guseva and Feudel 2017; Soos et al. 2008; Babler et al. 2015; Hill et al. 2001; Winterwerp 1998), a laboratory study (Alldredge et al. 1990) using natural aggregates collected from the ocean's surface layer (10-15 m depth) found that turbulent kinetic energy dissipation rates as strong as 10^{-4} W kg^{-1} did not cause aggregate breakup. Estimates of drag forces on falling aggregates (Hill et al., 2001) have further suggested that sinking-induced stresses may be more effective in causing aggregate breakup than turbulence. The conclusion from these studies (Alldredge et al. 1990;

Hill et al. 2001) was that disaggregation by turbulence was relatively unimportant in the upper ocean. Experimental (Soos et al. 2008) and numerical studies (Babler et al. 2015) investigating the collision of small particles (<~100 μm) have since shown that turbulence initially enhances aggregation, but disaggregation becomes increasingly important in controlling aggregate size distribution as the system ages and aggregates grow. More recent observations of aggregates made in the coastal benthic boundary layer (Mikkelsen et al. 2006; Safak et al. 2013) and energetic tidal channels (Braithwaite et al. 2012; Bowers et al. 2007) have shown that turbulence may indeed cause aggregate breakup, thereby limiting the size distribution of aggregates formed, reinstating the likely importance of disaggregation by turbulence.

The general applicability of these studies to understanding aggregation processes in the upper layers of the ocean remains uncertain for several reasons. First, the biological composition of marine aggregates that affects aggregation and disaggregation processes is known to be highly sensitive to changes in the ambient environmental conditions and the methods used for collection (Alldredge and Gotschalk 1988). For example, the stickiness of diatoms following collection from the field has been shown to increase due to nutrient and light limitation (Kiørboe et al. 1990; Kiørboe 2000; Engel 2000). Aggregates become compacted under even most gentle collection methods, potentially leading to stronger bonds

(Alldredge and Gotschalk 1988), which may be the reason aggregates survived the strong turbulence generated in the laboratory experiments (Alldredge et al. 1990). Aggregates in the benthic boundary layer tend to be much smaller than the marine aggregates observed in the upper ocean water column; in part because their composition contains a higher density of the minerals and sediments (Larsen et al. 2009). In comparison, the composition of aggregates formed in the ocean surface layer contains an increased fraction of organic material, including living and dead phytoplankton (Simon et al. 2002; Silver and Shanks 1978), faecal pellets (Turner 2015) and extracellular polymeric substances (EPS) (Bhaskar and Bhosle 2005).

Another important difference between laboratory experiments, energetic coastal environments (e.g., bottom boundary layer, tidal channels) and the upper water column of the open ocean is the intensity of turbulence. Turbulent kinetic energy dissipation rates in the upper water column rarely exceed 10^{-6} W kg^{-1}, except in the top few meters of surface layer when breaking surface waves (Geyer et al. 2008; Smyth and Moum 2019) generate strong turbulence. Similarly, kinetic energy dissipation rates can far exceed 10^{-5} W kg^{-1} in laboratory experiments and in the bottom boundary layer of coastal environments, where waves and currents can generate intense near-bed turbulence (Geyer et al. 2008). As a result, the relationship observed between turbulence and aggregates in highly localized bottom

boundary layers (Mikkelsen et al. 2006; Safak et al. 2013) and energetic coastal waters (Braithwaite et al. 2012; Bowers et al. 2007) are not likely to be representative of processes occurring in the water column interior of the upper ocean that occupies most of the world ocean.

These uncertainties support the necessity of field measurements in the upper ocean to develop our understanding of the relationship between turbulence and aggregates and its implications for the biological pump under climate change (Irwin et al. 2015). In this chapter, I collected simultaneous measurements of turbulence and aggregates in the upper ocean (~10-100 m) away from energetic coastal environments. I explore how aggregate size and other related properties, such as morphology and volume concentration, are affected by turbulence in the sunlit upper layer of the world ocean where particles are formed by primary production.

2.2 Method

2.2.1 Observation site

Laboratory of ocean ecosystem dynamics lead by Prof. Yamazaki made a series of non-disruptive measurements of turbulence and aggregates in the upper ocean water column,

between the surface and 100 m. Measurements were made during 10 campaigns and multiple seasons in coastal and offshore waters of Japan (Table 2.1).

2.2.2 TurboMAP-L

Microscale variations in temperature and turbulent velocity were measured with a free-fall microstructure profiler (TurboMAP-L, JFE Advantech Co., Ltd., Figure 2.1, Table 2.2, (Doubell et al. 2009) at a sample rate of 512 Hz and a fall-speed of ~0.5 m s^{-1}. I estimated the rate of turbulent kinetic energy dissipation (ε, W kg^{-1}) by integrating the turbulent velocity shear spectrum obtained from a shear probe over 2 second segments (~ 1m) from approximately 1 cycle per meter to half the Kolmogorov wavenumber ($(\nu^3/\varepsilon)^{1/4}$) (Doubell et al. 2014; Kokubu et al. 2013), where ν is the kinematic viscosity of seawater. A correction was applied to recover the unresolved variance of velocity shear spectrum (Oakey and Elliott 1982) using the Nasmyth empirical spectrum (Nasmyth 1970). The size of the shear probe that measures turbulent velocity was designed to resolve an expected minimum level of $\varepsilon \sim 10^{-10}$ W Kg^{-1} (Lueck et al. 2002) under the assumption of isotropic turbulence (Tennekes and Lumley 1972). Although turbulence may not be isotropic when ε is low, axisymmetric turbulence theory that accounts for stratification effects on turbulence indicates the error associated with use of the isotropic turbulence theory is less than 35%

(Yamazaki and Osborn 1990). Therefore, ε estimates based on the isotropic turbulence theory are a reasonable approximation to its true value. To avoid contamination by vessel-generated turbulence, I discarded ε observations obtained within 10 m of the surface. Increases in the 1 m scale turbidity or ε were used to detect the presence of bottom boundary layer in waters less than 100 m deep. Since these signals were typically detected much closer than 10 m from the bottom, I discarded observations made within the bottom 10 m of all profiles to avoid contaminating water column observations without those from benthic boundary layers.

2.2.3 DSL camera

A mini CMOS camera (DSL II 190, Little Leonard Inc., Figure 2.1.c) (Doubell et al. 2009) mounted on TurboMAP-L collected images of aggregates at a sampling rate of 5 Hz simultaneously with shear observations. Processed images had a field of view of 2 cm × 2 cm and a pixel resolution of 59 μm (Doubell et al. 2009). Streaked images were identified by assessing the 2D image spectrum using a 2D Fast Fourier Transform (2D FFT) (Doubell et al. 2009; Franks and Jaffe 2001). The 2D spectrum is a symmetric circle when images are not smeared, whereas asymmetry is seen in the 2D spectrum of streaked images. To test for asymmetry, two perpendicular sets of 1D spectra were chosen and the ratio of

variance for each wavenumber was calculated for each perpendicular pair. The variance ratio is approximately 1 in unstreaked images, with images rejected from further analysis if the average variance ratio for one perpendicular pair exceeded 1.5 or 1/1.5. This criterion assesses smearing across all aggregates imaged in the field of view and minimizes the rejection of images which contain rare individual long and thin aggregates.

Individual aggregates were then approximated as ellipses using the *regionprops* function in MATLAB (Mathworks Inc.) to determine major (*MajAL*) and minor (*MinAL*) axis lengths and equivalent spherical diameters (*ESD*). To focus on the larger size fraction of aggregates expected to be influenced by turbulence (McCave 1984), only objects with *MajAL* > 0.03 cm were considered to be aggregates. Coincident high-resolution fluorescence microstructure profiling that resolved millimetre scale changes in chlorophyll-*a* fluorescence showed extremely strong signals where aggregates were seen (Doubell et al. 2009), implying that aggregates captured by the DSL camera contained live phytoplankton. Additional laboratory tank experiments using particles of known size were also conducted to confirm that unfocused particles and streaked images were removed by the size threshold and 2D spectrum criteria. In total, 57,669 images collected over 148 profiles were retained. A total of 1,269,978 aggregates were identified; among them 1,103,412 aggregates were observed for $\varepsilon < 10^{-6}$ W kg^{-1} and 166,566 aggregates for $\varepsilon > 10^{-6}$ W kg^{-1}.

Relationships between turbulence and aggregates were then examined using 10 m scale average properties that included, the average turbulent kinetic energy dissipation rate ($\bar{\varepsilon}$, W kg^{-1}), total aggregate volume concentration (V_{agg}, ppm), aggregate minor axis length ($\overline{MinAL}$, cm), major axis length ($\overline{MajAL}$, cm), equivalent spherical diameter ($\overline{ESD}$, cm) and aspect ratio ($\overline{AR} = \frac{\overline{MajAL}}{\overline{MinAL}}$), where the over bar represents the 10 m scale mean value. Since the imaging system provides a 2D image of a 3D object, differences in aggregate size due to orientation are expected to be reduced by the use of 10 m scale average metrics. The volume of an individual aggregate is calculated as $\frac{\pi}{6}ESD^3$, where V_{agg} is the fraction of volume occupied by aggregates and is expressed in cm^3 m^{-3}, equivalent to parts per million (ppm).

Aggregate number spectra (Petrik et al. 2013) (n) were used to describe the size distribution of aggregates. The number of aggregates (ΔN) in logarithmically increasing *MajAL* bins of average size d was divided by the bin width (Δd) and the sample volume to construct a number spectrum. Any ΔN<10 was discarded before computing n. For each spectrum, a bilinear relationship was fit to log(n) as a function of log(d) to obtain values for the inflection point (L_{int}) and the slope below (slope 1, small aggregates) and above (slope 2, large aggregates) the L_{int}. The mean sum of squared error of each fit was then calculated. Different L_{int} was then selected at intervals of Δd either side of the first L_{int} and the slopes

determined. The final accepted L_{int} and slopes were those with the smallest mean sum of squared error.

Finally, the distribution of aggregate volume as a function of the ESD size expressed as the normalised volume distribution *nVd* (Petrik et al. 2013; Jackson et al. 2015) was estimated for each order of magnitude of $\bar{\varepsilon}$ of between $10^{-10} < o(\bar{\varepsilon}) < 10^{-5}$ W kg^{-1}. For each $o(\bar{\varepsilon})$ interval, the number of aggregates in logarithmically increasing *ESD* bin sizes (*d*) was divided by the bin width (Δd) and sample volume to construct an *ESD* number spectrum. *ESD* number spectra were multiplied by $V=\frac{\pi}{6}ESD^3$ and *d* to obtain *nVd*, whereby the integral of *nVd* is equivalent to $V_{agg} = \int nV \, \mathrm{d}d = \int nVd \, \mathrm{d}(\ln d)$.

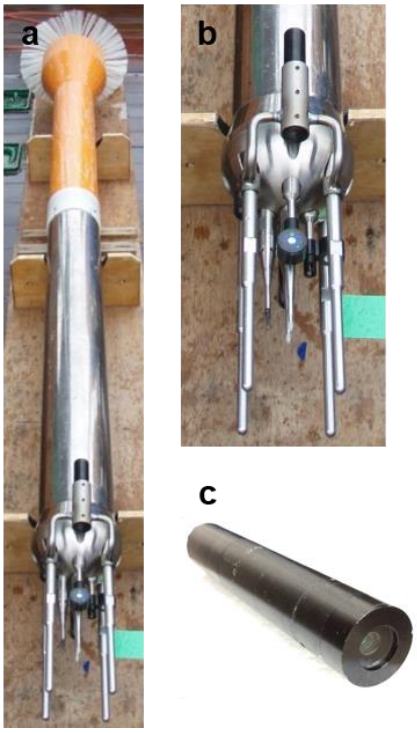

Figure 2.1 TurboMAP L and DSL camera. (a) TurboMAP-L (b) DSL camera mounted on TurboMAP-L (c) DSL camera

Table 2.1 Aggregate size and abundance at each site

	Major axis length [cm]						
	Min.	Max.	Mean	SD	Picture	Particles	Abundance [cm^{-3}]
Kuroshio09	0.03	0.99	0.06	0.05	18455	94802	0.64
Kuroshio13	0.03	1.22	0.06	0.04	21771	202795	1.16
Miyake	0.03	1.16	0.08	0.06	5944	48471	1.02
Oshima	0.03	1.65	0.08	0.07	13238	90213	0.85
Otsuchi	0.03	0.91	0.08	0.05	4187	135168	4.04
Joga	0.03	1.96	0.1	0.09	8466	241919	3.57
Tateyama	0.03	1.17	0.09	0.07	2289	88001	4.81
Tokyo Feb	0.03	1.5	0.11	0.1	2491	226566	11.3
Tokyo Sep	0.03	1.3	0.09	0.08	4860	234666	6.04
Biwa	0.03	0.86	0.07	0.05	5950	183067	3.85

Table 2.2 TurboMAP-L specification

Parameters	Range	Accuracy	Resolution	Sampling rate [Hz]
Shear[s^{-1}]	0 to 4	5%	0.0001	512
Fast temperature[degC]	-5 to 45	±0.01	<0.0001	512
Slow temperature[degC]	-5 to 45	± 0.05	0.001	64
Conductivity[mS^{-1}]	0 to 70	± 0.01	0.002	64
Pressure [m]	0 to 500	0.2%	0.01	64
Accelerometers[G]				
- X			0.0005	256
- Y	±1	1%	0.0005	256
- Z			0.0005	64
Fluorescence				
- LED [ugL^{-1}]	0 to 100	±0.5	0.005	256
- Laser	0 to 100	±0.5	0.005	256
Turbidity[ppm]	0 to 100	±1	0.0005	256

2.4 Results

2.4.1 Turbulence and aggregate size and volume concentration

Values of $\bar{\varepsilon}$ ranged from 10^{-10} to 10^{-5} W kg^{-1} (Figure 2.2.a) and spanned the full range of naturally occurring turbulence intensities found in the upper ocean interior, away from energetic surface and bottom boundary layer regions (Geyer et al. 2008; Smyth and Moum 2019). Aggregate $\overline{MajAL}$ ranged between 0.031 and 0.133 cm and $\log_{10}(\overline{MajAL})$ and was positively correlated with $\log_{10}(\bar{\varepsilon})$ (Figure. 2.2.a, $r^2 = 0.52$, $n = 567$, $p << 0.001$). The

majority of ($\overline{MajAL}$) were smaller than the size of the smallest turbulent eddies, here defined by the Kolmogorov length scale ($L_k = (\nu^3/\varepsilon)^{1/4}$). Positive correlation between $\log_{10}(\overline{MajAL})$ and $\log_{10}(V_{agg})$ (Figure 2.2.b, $r^2 = 0.74$, $n = 567$, $p << 0.001$) indicates that V_{agg} is also a crucial factor determining the size distribution of aggregates, since aggregate total volume is a measure of the number of particles available for coagulation (Jackson 1990). Higher particle concentrations should increase coagulation rates, leading to larger particles, while sinking and disaggregation prevent particles from becoming indefinitely large. Multiple linear regression analysis showed that $\log_{10}(\bar{\varepsilon})$ and $\log_{10}(V_{agg})$ collectively explained 81% of the variance in $\log_{10}(\overline{MajAL})$ ($r^2 = 0.81$, n=567, p<<0.01), with $\log_{10}(\bar{\varepsilon})$ contributing 32% and $\log_{10}(V_{agg})$ 68% to this correlation.

2.4.2 Aggregate size distribution

The results show 97% of $\overline{MajAL}$ values were below 0.1 cm in size (Figure 2.2.a), which is the size L_k for $\bar{\varepsilon} = 10^{-6}$ W kg^{-1} and the upper limit of dissipation rates typically observed in the ocean interior (Geyer et al. 2008; Smyth and Moum 2019). The positive correlation observed at length scales smaller than L_k demonstrates that turbulence enhancement of aggregation occurs at higher rate than disaggregation when shear is laminar (Braithwaite et al. 2012) and aggregate sizes are smaller than L_k. This fact results in the net formation of

larger aggregates. When the flow scale is equal to the Kolmogorov scale, the Reynolds number is 1 and the flow is very viscous, hence the resulting flow at this length scale is laminar shear (Tennekes and Lumley 1972). Previous bottom boundary observations have shown a decrease in aggregates size when L_k was smaller than 0.1 cm, equivalent $\varepsilon > 10^{-6}$ W kg^{-1} (Braithwaite et al. 2012). Therefore, I expect that for $\bar{\varepsilon} > 10^{-6}$ W kg^{-1} and $\overline{MajAL} < L_k$the disaggregation rate exceeds the aggregation rate, as shear associated with the smallest turbulent eddies causes breakup and inhibits further size increases.

While values of $\overline{MajAL}$ shown in Figure 2.2 were calculated using 10 m averages, the number of individual aggregates with *MajAL* larger than L_k remained relatively small. Above $\bar{\varepsilon} \geq 10^{-6}$ W kg^{-1}, 63% of individual *MajAL* sampled (non-averaged samples, *n*=166,566) were smaller than L_k. At lower turbulent intensities, the proportion of individual aggregates smaller than L_k increased from 80% at $\bar{\varepsilon} = o(10^{-7}$ W kg$^{-1})$ to 99% of aggregates at $\bar{\varepsilon} = o(10^{-10}$ W kg$^{-1})$. This shift demonstrates that aggregate size distribution is a dynamic property, with the potential for some aggregates to increase in size even under high average turbulent intensities ($\bar{\varepsilon} > 10^{-6}$ W kg^{-1}) and for others to undergo disaggregation at lower average turbulent intensities ($\bar{\varepsilon} < 10^{-6}$ W kg^{-1}). This interpretation is supported by results shown in Figure 2.3, which demonstrates increases in the variability of individual aggregate

sizes around the mean, expressed as the coefficient of variation, (CV_{MajAL} = standard deviation/mean), under increasing turbulent intensities.

For a more direct comparison between turbulence and aggregate size I calculated the mean size of individual aggregates for each order of magnitude of $\bar{\varepsilon}$ ($\overline{MajAL_{\varepsilon}}$, cm). Increases in $\overline{MajAL_{\varepsilon}}$ dropped from ~20% between $\bar{\varepsilon}$ = $o(10^{-10}$ W kg^{-1}) and $o(10^{-9}$ W kg^{-1}) to ~10% between $\bar{\varepsilon}$ = $o(10^{-7}$ W kg^{-1}) and $o(10^{-6}$ W kg^{-1}) (Figure 2.3.a) and were associated with a corresponding increase in the coefficient of variation (CV_{MajAL}) from 0.69 to 0.98 (Figure 2.3.b). The plateau in CV_{MajAL} observed at higher turbulent intensities is consistent with disaggregation rates increasing as both turbulence levels and the average size of aggregates increase (Figure 2.2.a).

2.4.3 Turbulence and shape of aggregate

Increases in aggregate size with turbulence were also associated with changes in aggregate morphology (Figure 2.4). The increase in ($\overline{AR}$) with $\log_{10}(\overline{MajAL})$ (Figure 2.4.a ; r^2 = 0.45, n = 567, p<< 0.001) and $\log_{10}\bar{\varepsilon}$ (Figure 2.4.b; r^2 = 0.40, n = 567, p << 0.001) shows that aggregates became elongated with increases in size and turbulence intensity. Numerical simulations and laboratory experiments (Eaton and Fessler 1994; Squires and Eaton 1991; de Jong et al. 2010) have shown that inertial particles in turbulence cluster in

regions of high-strain. The current results suggest that larger aggregates become inertial, possibly being strained by shear due to strong turbulence, resulting in elongation. Whilst increased inertial force on larger aggregates may also enhance breakage under strong turbulence, laboratory experiments (Ruiz et al. 2004) and numerical simulations (Clifton et al. 2018) have demonstrated the settling velocity of elongated phytoplankton increase under elevated turbulence. It is possible that aggregate settling velocity increases due to both morphological changes (Figure 2.4.b) and size increases (Figure 2.2.a, Figure 2.3) under increasing turbulence up to a critical turbulent intensity, $\bar{\varepsilon} = 10^{-6}$ W kg^{-1}.

Aggregate number spectrum (n, cm^{-4}) (Petrik et al. 2013) as a function of $\log_{10}(MajAL)$ describes the non-averaged size distribution of individual aggregates throughout the water column. Figure 2.5 shows a spectrum for individual aggregates sampled between 10 and 100 m depth from the Kuroshio extension (37˚04′05″N, 142˚54′36″E). Here, an average dissipation rate ε_{CA} was computed from all individual ε to estimate the corresponding mean Kolmogorov scale ($L_{k,CA}$, cm) in these near surface waters (Figure 2.5, dashed lines). Two slopes were fitted to the number spectrum (Figure 2.5, solid lines), with a gradient of -2.72 for the smaller aggregate size range (slope 1) and -4.53 for the larger aggregate size range (slope 2). There was a decrease in the number of aggregates expected by using the line fit to the smaller aggregates for aggregates larger than the intersection (L_{int}, cm) of the two lines.

Here, L_{int} is 0.16 cm and the Kolmogorov scale based on ε_{CA} is $L_{k,CA}$ = 0.17 cm. The ratio between L_{int} and $L_{k,CA}$ is 0.95 and shows the number of aggregates decreases significantly when aggregate size is larger than $L_{k,CA}$. This trend was consistent across all campaigns used in this study (Appendix Figure A and Table A). The significant decrease in *n* as the aggregate size exceeds $L_{k,CA}$ suggests that the role of particle collision in aggregate formation becomes smaller as disaggregation due to turbulence becomes more prominent.

The normalized volume distribution (*nVd*, ppm) (Petrik et al. 2013; Jackson et al. 2015) as a function of $\log_{10}(ESD)$ provides further insight into aggregation and disaggregation processes (Figure 2.6). The shape of the *nVd* distributions is similar to the lognormal distributions described previously (Petrik et al. 2013). A simulation (Jouandet et al. 2014) showed that *nVd* for aggregates have a lognormal-like distribution when both aggregation and disaggregation are taken into account, suggesting that disaggregation occurs at all level of turbulence (Figure 2.6). This is consistent with the original breakage model proposed by Kolmogorov (1941b). Lognormal turbulence theory (Kolmogorov 1941b; Gurvich and Yaglom 1993) shows that a fraction of the water over which $\bar{\varepsilon}$ is calculated contains localized regions of the turbulent kinetic energy dissipation rate higher than ensemble average (Yamazaki and Squires 2003). Hence, for the range of observed $\bar{\varepsilon}$, parcels of highly localized turbulence may exceed $\varepsilon = 10^{-6}$ W kg^{-1} and are expected to cause disaggregation

even under conditions of low average dissipation rates. The area under the curve of *nVd* is proportional to V_{agg} (Petrik et al. 2013; Jackson et al. 2015). Increased *nVd* with $\bar{\varepsilon}$ is consistent with the aggregation rate increasing under stronger turbulence. The distribution peak shifted to larger *ESD* with increasing in $\bar{\varepsilon}$ by ~15-20% when $\bar{\varepsilon}$ increased one order of magnitude. The increase was limited to ~0.16 cm when $\bar{\varepsilon} = 10^{-6} - 10^{-5}$ W kg^{-1}. For *ESD* larger than the distribution peak, negative *nVd* slopes indicate that loss of the large aggregates by disaggregation counters their production by aggregation; steeper slopes at higher $\bar{\varepsilon}$ show that the loss becomes more rapid as the turbulence intensity increases. This is consistent with turbulence-induced disaggregation rate overtaking the aggregation rate with increased V_{agg}.

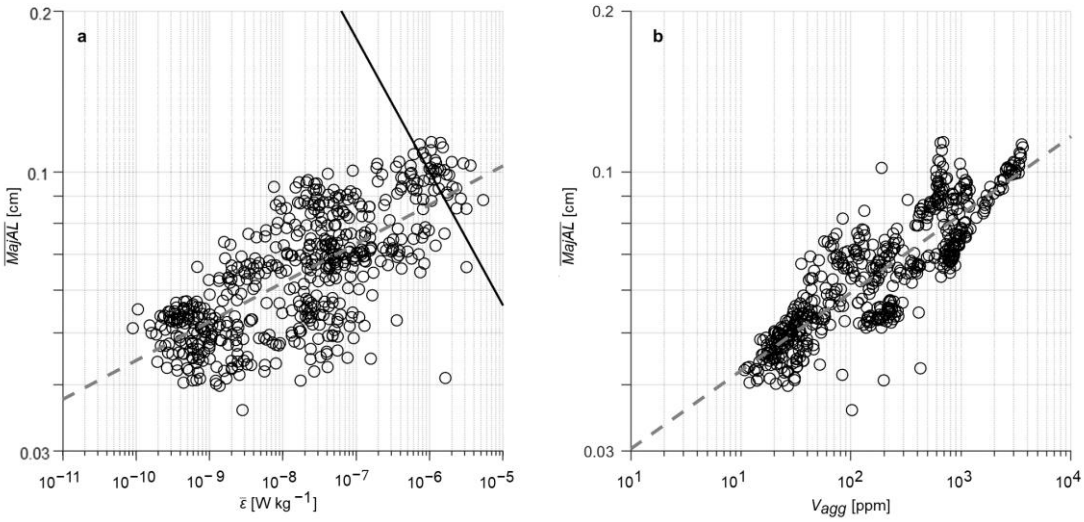

Figure 2.2 Changes in average major axis length ($\overline{MajAL}$, cm) of aggregates (n=567) with corresponding measures of; (a) average turbulent kinetic energy dissipation rate ($\bar{\varepsilon}$, W kg^{-1}) and (b) total aggregate volume concentration (V_{agg}, ppm). All values were calculated over 10-m depth intervals. The black solid line in (a) shows the Kolmogorov length scale and grey dashed lines in (a) and (b) indicate regression lines.

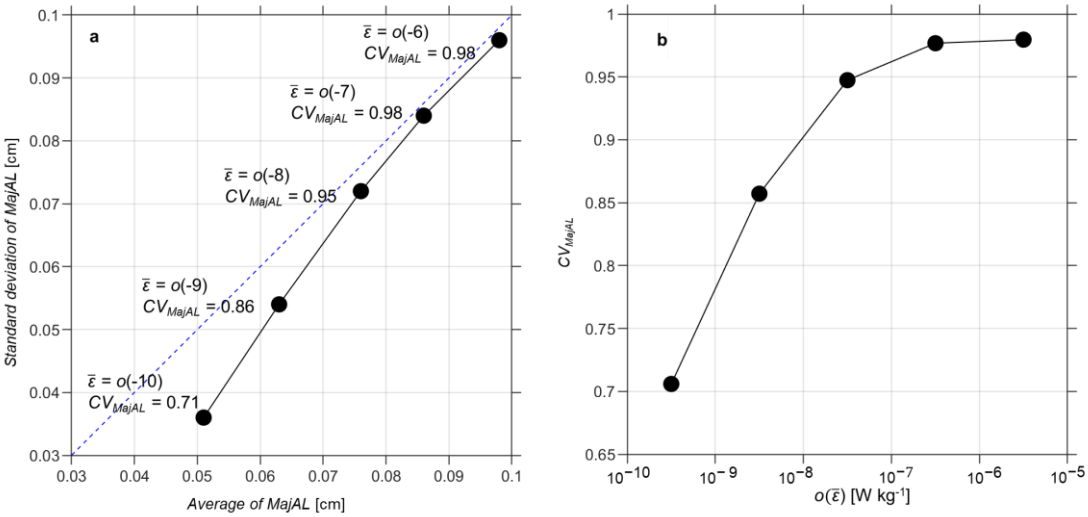

Figure 2.3 Aggregates were sorted into 5 turbulence ranges based on corresponding ε; (a) individual aggregates within each range were used to calculate mean and standard deviation of *MajAL*. Blue dashed line indicates where CV_{MajAL}, given by $\frac{Standard\ deviation}{Mean}$, is 1. CV_{MajAL} and $o(\bar{\varepsilon})$ for each point are annotated. The total number of aggregates, average size and standard deviation and CV_{MajAL} for each turbulence range were: $o(\bar{\varepsilon}) = 10^{-10}$) 182493, 0.051, ± 0.036 cm, 0.71; ($o(\bar{\varepsilon}) = 10^{-9}$) 164335, 0.063 ± 0.054 cm, 0.86; $o(\bar{\varepsilon}) = 10^{-8}$) 471271, 0.076 ± 0.072 cm, 0.95; ($o(\bar{\varepsilon}) = 10^{-7}$) 284695, 0.086 ± 0.084 cm, 0.98 and ($o(\bar{\varepsilon}) = 10^{-6}$) 166566, 0.098 ± 0.096 cm, 0.98, respectively. (b) CV_{MajAL} increased as $o(\bar{\varepsilon})$ increased.

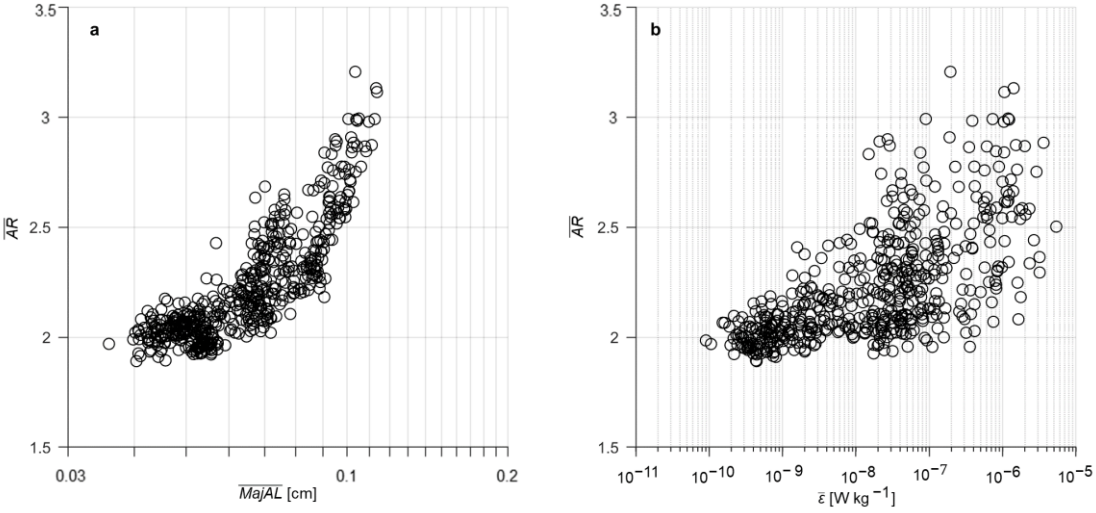

Figure 2.4 Relationship between the average aspect ratio ($\overline{AR}$) of aggregates (n = 567) with corresponding average values of; (a) major axis length ($\overline{MajAL}$, cm) and (b) the turbulent kinetic energy dissipation rate ($\bar{\varepsilon}$, W kg^{-1}). All values were averaged over 10 m depth intervals.

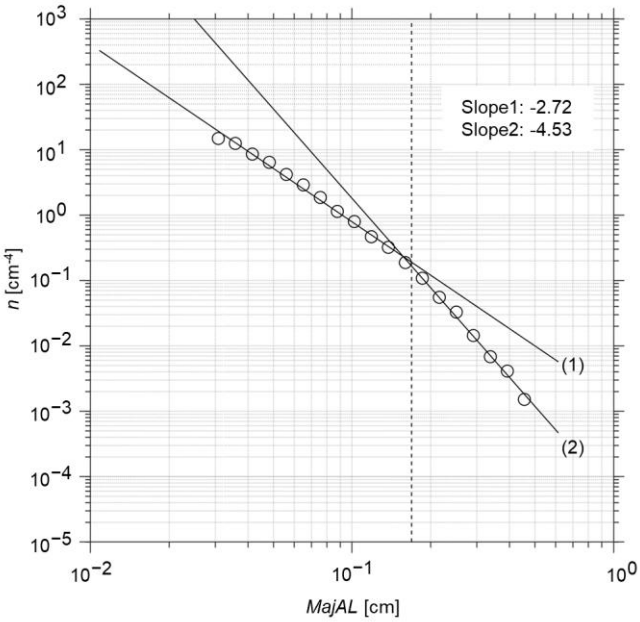

Figure 2.5 Number spectrum (n, cm^{-4}) shows the aggregate size distribution over logarithmically increasing *MajAL* (cm) size classes. Data were from the Kuroshio

extension (37˚04′05″N, 142˚54′36″E) where maximum water depth exceeded 5000 m. All individual aggregates sampled in depths 10- 100 m (total 17,526 aggregates) were used to construct *n*. Dashed line indicates L_k= 0.17 cm based on the cruise average dissipation rate ($\overline{\varepsilon_{CA}}$ = $o(10^{-7}$ W kg^{-1}). The fitted slopes are -2.72 (slope 1) and -4.53 (slope 2) and the intersection between the two lines L_{int} is 0.16 cm

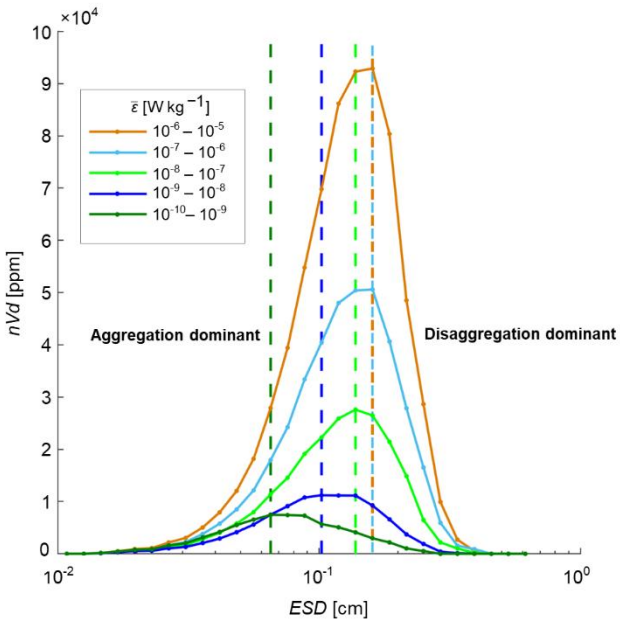

Figure 2.6 Changes in the normalised volume distribution (*nVd*, ppm*)* of aggregates as a function of equivalent spherical diameter (*ESD*, cm) for 5 orders of turbulent kinetic energy dissipation rate ($\boldsymbol{o}(\bar{\varepsilon})$, W kg^{-1}) measured in the upper (10 - 100 m) ocean. Vertical dashed lines indicate the mode for each lognormal *nVd* distribution. Aggregation dominated below the mode and disaggregation above the mode.

2.5 Conclusion

This study provides a comprehensive set of simultaneous measurements of aggregate concentrations as a function of size that resolve the full range of turbulent intensities, $\bar{\varepsilon}$ =

10^{-10} – 10^{-6} W kg^{-1}, found within the upper ocean away from energetic near surface and bottom boundary layers (~10-100 m depth). Although turbulent intensities in coastal environments and near boundary layers can far exceed 10^{-5} W kg^{-1}, our observed values cover the range of intensities found typically over the majority of world upper ocean surface layer (Geyer et al. 2008; Smyth and Moum 2019). This study shows turbulence enhances aggregation up to ~$\bar{\varepsilon}$ = 10^{-6} W kg^{-1} with greater turbulence intensities cause increasing disaggregation, consistent with laboratory (Dyer and Manning 1999) and theoretical (Ruiz and Izquierdo 1997; Winterwerp 1998) studies and the early conceptual view of aggregation dynamics studied in coastal environments (Dyer 1989). Since most of the ocean upper water column interior contains $\bar{\varepsilon}$ < 10^{-6} W kg^{-1} (Geyer et al. 2008; Smyth and Moum 2019), turbulent mediation of aggregate size and morphology is likely to be an important factor influencing a range of biogeochemical processes, including carbon sequestration. This is because aggregate size and morphology are important determinant factors of settling velocities and carbon flux (Alldredge 1998; Laurenceau-Cornec et al. 2015), microbial abundances (Kiorboe et al. 2003; Kiørboe 2003) and associated biogeochemical activity through bacterial remineralization (Kiørboe 2003; Simon et al. 2002; Azam and Long 2001). As climate change is expected to supress turbulence intensity (Passow and Carlson 2012) and alter phytoplankton communities (Falkowski and Oliver

2007; Irwin et al. 2015) in the euphotic zone, the mediation of aggregates by turbulence may have unexpected consequences for global carbon cycle via the biological pump (Gehlen et al. 2006).

Chapter 3. Aggregate as a hotspot of phytoplankton: Comparison between aggregate and laser fluorescence data

3.1 Introduction

Marine aggregate was, historically, recognised as a community of dead organic materials when it was first collected and observed by a microscope (Tsujita 1953). Recent studies, in contrast, have shown that aggregate contains live organisms (Azam 1998; Shanks and Trent 1979; Silver and Shanks 1978),with organic and inorganic contents such as chlorophyll-*a*, particulate organic carbon an nitrate. Because of their biological makeup, aggregate plays an important role in marine ecosystems. For example, individual aggregate accommodate many different organisms and becomes hotspots of microbial activities (Simon et al. 2002). Aggregate also comprises an important nutrient source to oligotrophic waters (Shanks 2002); nutrient-rich water is trapped inside aggregate during their formation and it is delivered to deeper water as aggregate sinks. Aggregate can attract organisms, particularly when nutrients inside leak out during its erosion. Furthermore, experimental studies (Larson and Shanks 1996; Kiørboe 2001) have shown that various fish and copepod feed on aggregate directly. Despite such biological importance, few in-situ observations have been used to directly compare aggregate to biological parameters.

In this study, images of aggregate and fluorescence is collected from 10 different fields around Japan. Direct comparison between aggregate sizes and fluorescence signals will be shown to investigate the relationship between fluorescence signals and aggregate sizes, using *in-situ* field data. Furthermore, contrasts will be described between aggregate in open water and coastal water.

3.2 Method

3.2.1 TurboMAP-L and laser fluorescence probes

Microscale variations in temperature and turbulent velocity were measured with a free-fall microstructure profiler (TurboMAP-L, JFE Advantech Co., Ltd.) at a sampling rate of 512 Hz and a fall-speed of ~0.5 m s^{-1}. See Method 2.2.1 for more details.

As described in section 2.2.1 and Table 1, TurboMAP-L carries 2 fluorescence probes using different light sources. A laser fluorescence probe resolves ~2 mm (Doubell et al., 2009) while a LED fluorescence probe resolves ~ 2 cm (Wolk et al., 2001). Previous studies that compared vertical profiles obtained by the laser fluorescence probe and the LED fluorescence probe have shown that the laser fluorescence probe acquired intermittent strong signals which were not obtained by the LED fluorescence probe (Doubell et al. 2009). Since averaged profiles agreed, it was concluded that the laser fluorescence probe was detecting smaller scale phytoplankton distribution. They also found that aggregates were more abundant in depth where laser fluorescence signals showed intermittent

features, suggesting that the intermittent strong signals were from individual aggregates. Thereby, in this study, the laser fluorescence probe that resolves ~2 mm scale is used for comparison with aggregate distribution, assuming that the strong signals acquired by the laser probe are signals from aggregates. Since intermittent features obtained from the laser probe is lost when vertical profiles are averaged over depth, strong signals that exceed a certain threshold were integrated over 10 meters instead of taking average (Foloni-Neto et al. 2014). In order to extract intermittent signals as seen in Figure 3.1.a, a threshold was set at 1.5 times of 1 metre moving average. Red dashed lines in Figure 3.1.b, c and d show 1 metre moving average and solid lines indicate the threshold. Signals exceeded the threshold were integrated for every 10 metres (red triangles in Figure 3.1.c and d) and integrated values are called integrated laser fluorescence intensity (*ILFI*, μg L^{-1}/10m) in this study.

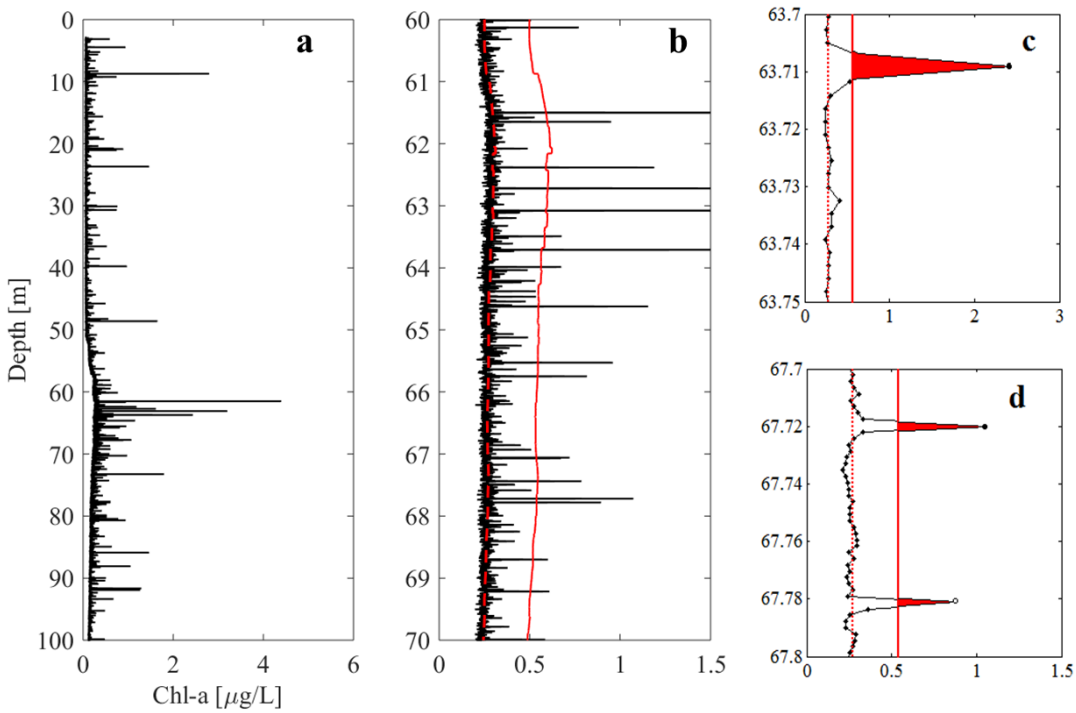

Figure 3.1 Integrating method of laser fluorescence data: a) A row profile of laser fluorescence signals. b) A threshold over 10 metres. A red dashed line is 1 metre moving average and a red solid line is 1.5 times of 1 metre moving average. The red solid line is used as a threshold to separate intermittent signals. b and c) Examples of signals that exceeded the threshold. The areas under ted triangles were integrated for every 10 metres.

3.2.2 DSL camera and aggregate measures

Images from DSL camera were used for aggregate measures. The detail description of DSL camera is given in Chapter 2 method section (2.1.2). In this Chapter, total volume concentration of aggregate (V_{agg}, ppm) over 10 metres which is a fraction of aggregate in water is used to compare with *ILFI*.

3.2.3 Number spectra

Aggregate number spectra (n) were used to describe the size distribution of aggregates. In order to explore the differences between open water and coastal water, number spectra for open water and coastal water were constructed independently. The number of aggregates (ΔN) in logarithmically increasing *MajAL* bins of average size d was divided by the bin width (Δd) and the sample volume to construct a number spectrum. Any $\Delta N<10$ was discarded before computing n. For each spectrum, a bilinear relationship was fit to log(n) as a function of log(d). Bilinear regression lines were fitted to each size spectra. In this study, coastal water and open water are separated by locations. Open water includes Kuroshio (2009 and 2013), Oshima and Jogashima. Coastal water includes Tokyo bay (September and February), Tateyama and Otsuchi. Lake Biwas is also included in category of coastal water for further investigation.

3.3 Results

3.3.1 Laser fluorescence signals

Vertical profiles from the Kuroshio extension (2009) is shown in Figure 3.2. Laser fluorescence signals showed highly intermittent features and strong signals were seen in surface mixed layers and thermocline. Aggregates showed higher abundance in the depth where fluorescence showed strong signals. This suggests that locally strong fluorescence

signals are results of detecting aggregate as a community of phytoplankton. In order to confirm that the source of these intermittent signals is an aggregate, strong intermittent signals were directly compared with aggregate in next section.

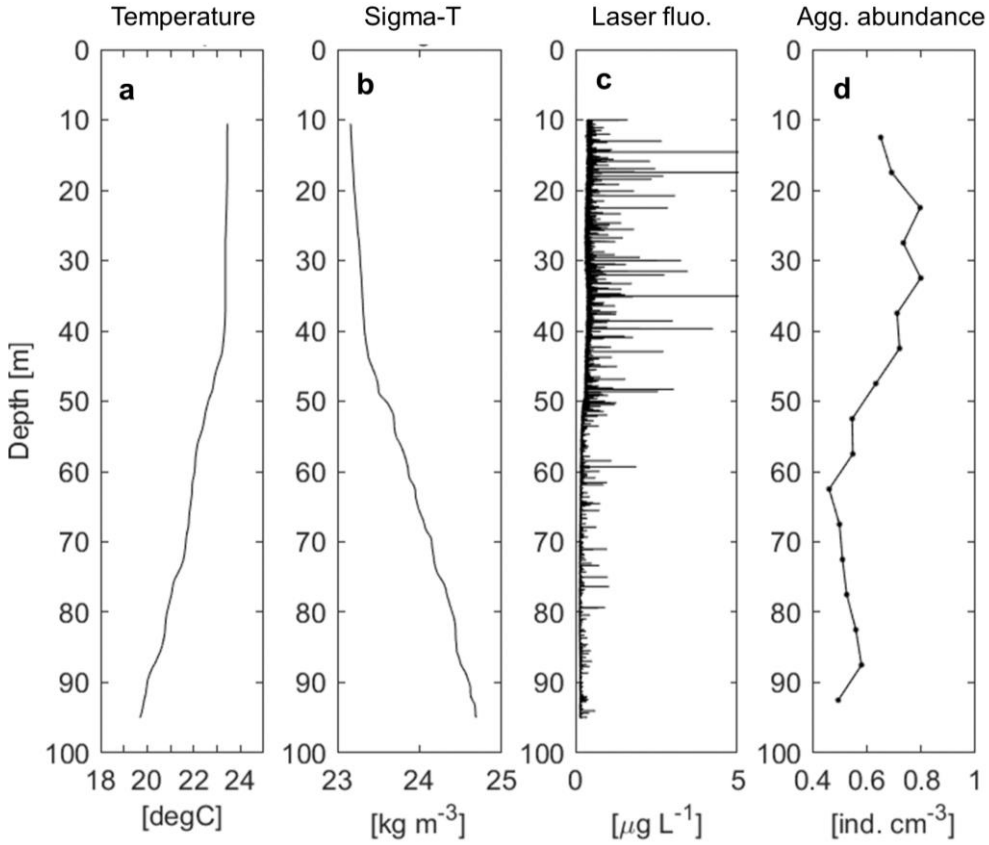

Figure 3.2 Vertical profile of (a) temperature, (b)density, (c) laser fluorescence and (d) aggregate abundance. Profile is obtained in Kuroshio extension in 2009 (37˚04′05″N, 142˚54′36″E). Aggregate abundance is calculated over 5 metres in order to provide distribution in finer vertical scale. Laser fluorescence showed stronger signals in surface mixed layer between 10 and 50 metres.

3.3.2 Integrated laser fluorescence intensity and aggregate

Strong signals were separated and integrated over 10 metres (*ILFI*, μg L^{-1}/10m). *ILFI* ranged widely in both open water and coastal water (Figure 3.3). *ILFI* reached 8.3×10^{3} μg L^{-1}/10m in open water and 3.9×10^{3} μg L^{-1}/10m in coastal water. The smallest *ILFI* obtained was 2.9×10^{-1} μg L^{-1}/10m in open water and 1.0×10^{-1} μg L^{-1}/10m in coastal water.

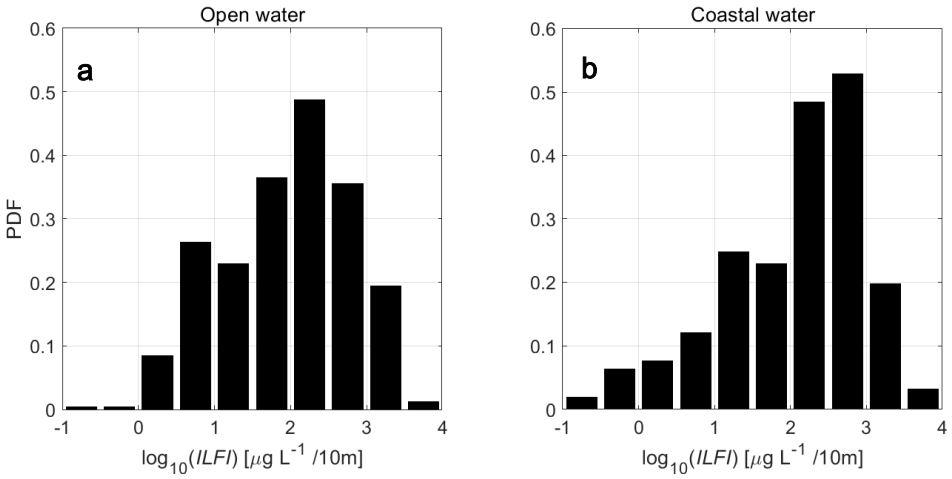

Figure 3.3 PDF of log-transformed integrated laser fluorescence intensity (ILFI, μg L^{-1}/10m). Both open water and coastal water had slightly left skewed distribution with skewness of -0.27 and -0.85 (n=472 and 314 respectively). Locations of open water and coastal water were defined in method section. 3.3.2 Integrated laser fluorescence intensity and aggregate

The integrated laser fluorescence intensity (*ILFI*, μg L^{-1}/10m) was compared with 10 metres averaged major axis length ($\overline{MAL}$, cm) and total volume concentration of aggregate over 10 metres (V_{agg}, ppm) to validate the source of signals are aggregate. Across 10 campaigns, $\overline{MAL}$ ranged between 0.04 -0.13 cm. Aggregate in coastal water was slightly

larger than that in open water but most aggregate was ranging in the same length scale (Figure 3.4.a). $\overline{MAL}$ and *ILFI* showed slight positive correlation over 10 data sets (r=0.37, p<<0.01, n=618). The correlation between $\overline{MAL}$ and *ILFI* was strong in coastal water (r=0.77, p<<0.01, n=227), while $\overline{MAL}$ and *ILFI* showed almost a weak correlation in open water (r=0.19, p<<0.01, n=391). Therefore, this fact suggests that aggregate contains more phytoplankton cells as it becomes larger in coastal water. However, phytoplankton is densely concentrated in aggregate regardless of the aggregate size in open water. This may be because sediment can also be the source of aggregate in coastal water. Small aggregate in coast may be sediment-rich ones that contains less phytoplankton cells.

V_{agg} was clearly smaller in open water than coastal water (Figure 3.4.b), showing that open water one is less occupied with aggregate. A strong positive correlation was found in coastal water data (r=0.70, p<<0.01, n=227), while the correlation was weak in open water data (r=0.25, p<<0.01, n=391). Figure 3.4.b shows more significant difference between open water aggregate and coastal aggregate. For a given *ILFI*, V_{agg} is smaller in open water than coastal water. This suggests that water column in coastal water needs to be more occupied with aggregate to obtain the same level of *ILFI* as open water case. Thus, phytoplankton is more densely concentrated in open water aggregate than coastal water aggregate. Although water column is less occupied with aggregates in open water,

individual aggregate carries highly concentrated phytoplankton as discussed above. The Kuroshio extension water is known as an oligotrophic and poor in productivities, however, this result suggests that productivities may be low on average but phytoplankton in hotspots (aggregates) are supporting the microscale ecosystems.

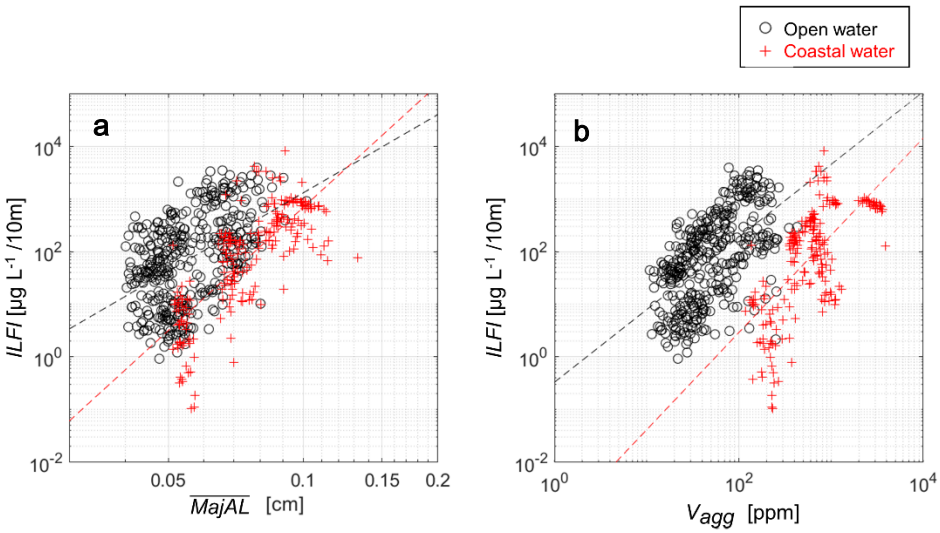

Figure 3.4 Comparison between *ILFI* and (a) 10m averaged major axis length ($\overline{MajAL}$, cm) and (b) total volume concentration of aggregate (V_{agg}, ppm). Black circles indicate open water (n = 391) and red cross indicates coastal water (n=227). Black and red dashed lines indicate regression lines.

3.3.3 Aggregate size distribution

In order to further investigate the difference in aggregate size between coastal water and open water, number spectra were constructed (Figure 3.5). Average *MajAL* in coastal water was 0.094 cm (*n*=811146) and 0.068 cm (*n*=292563) in open water, suggesting that

aggregates in coastal water are slightly larger than aggregates in open water, which is consistent with Figure 3.4.a. Larger *n* in coastal water shows that aggregate was more abundant in coastal water. This supports the result of Figure 3.4.b that shows that water column is more occupied with aggregate in coastal water than open water.

For both regions, bilinear regression lines were fitted; a slope over small aggregate is called slope 1 and a slope over large aggregate is called slope 2. For open water, slope1 ~ -2.34 and slope2 ~ -4.34, while slope1 ~ 1.68 and slope2 ~ -3.78 for coastal water. Less steep slopes for the coastal number spectrum show that aggregate distributes more evenly over different size classes, although large ones are less common. A steep slope for the open water number spectrum, however, shows that the difference in abundance is larger over size classes. Small *n* for large size class also shows aggregate becomes rarer when it becomes larger. Since water column is less occupied with aggregate in open water (Figure 3.4.b), particle collision rate that is an important parameter to control formation of aggregate (Jackson 1990) is expected to be low which may result in less large aggregate in open water.

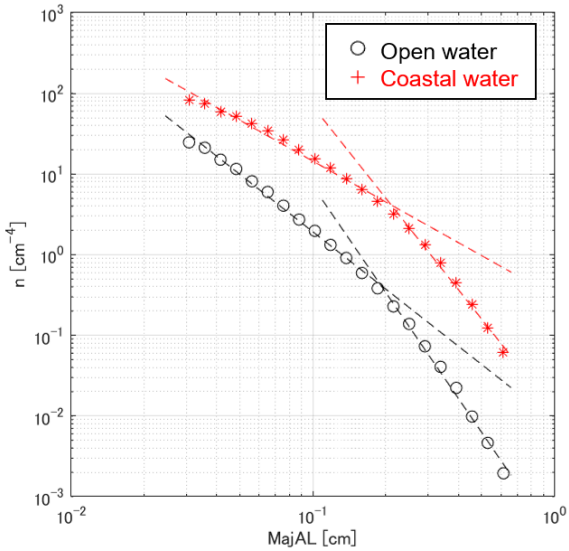

Figure 3.5 Aggregate number spectra as a function of major axis length (*MajAL*, cm); black circles indicate open water and red crosses indicate coastal water.

3.4 Conclusion

High abundance of aggregate was found in the surface mixing layer and thermocline where laser fluorescence showed strong signals (Figure 3.2), consistent with previous work (Doubell et al. 2009). This result indicates that the locally strong signals obtained by the laser fluorescence probe are likely detecting individual aggregates. Aggregates in coastal water were larger (Figure 3.4.a) and more abundant over different size classes (Figure 3.5) than the open water ones. V_{agg} was also higher in coastal water (Figure 3.4.b), showing that water is more occupied with aggregates. Although the data from bottom 10 metres is discarded to avoid resuspended sediment from bottom, turbidity in coastal water is higher

(Figure 3.6). Since the collision rate of particle increases with particle concentration, more aggregate is formed through collision in coastal water. Formation of large aggregate is more promoted when water column is more occupied with aggregate as discussed in Chapter 2.

Comparison of *ILFI* between coast and open water (Figure 3.4.a) showed higher V_{agg} of coastal water at given *ILF*, suggesting that phytoplankton is densely concentrated in open water aggregates. The Kuroshio is known as an oligotrophic environment with lower abundance of phytoplankton, however, it is possible that highly concentrated phytoplankton in aggregate is providing locally high productivity and supporting the local ecosystems.

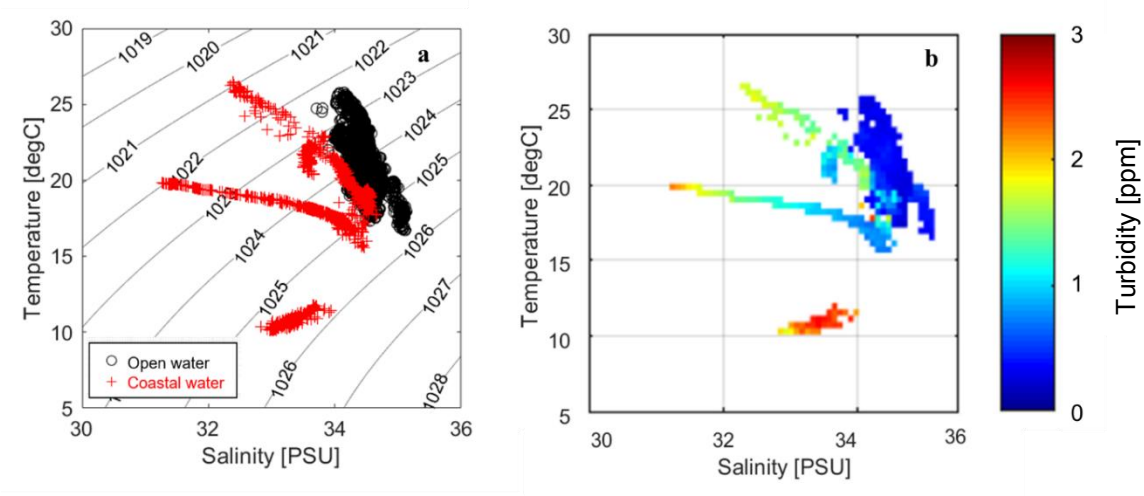

Figure 3.6 TS diagram. a: TS diagrams indicating open water (black circles) and coastal water (red crosses). Each variable is 1 m average. b: Turbidity indicated with colour on TS diagram. Turbidity is also 1 m average.

Chapter 4. Long term monitoring of aggregate using an observatory station

4.1 Introduction

Marine aggregate, formed through particle flocculation, is known to have significant impacts on marine ecosystems (Azam and Long 2001; Larson and Shanks 1996) and climate (Passow and Carlson 2012). Studies of aggregate were heavily based on laboratory experiments (Alldredge and Gotschalk 1988) and theoretical studies (Winterwerp 2002; Jackson 1990). Recently, imaging systems have been applied to collect vertical profiles of plankton such as Video Plankton Recorder (Gallager et al. 2004) and holographic systems (Owen and Zozulya 2000). These approaches can collect natural living organisms; however, it is still challenging to collect images of aggregate due to the fragile nature of aggregate. Unless the instruments are smoothly deployed with weak vibrations, the disturbance caused by instruments or the supporting frames can destroy fragile aggregates. A small digital still logger camera mounted on a microstructure profiler that travels vertically in free fall mode successfully recorded aggregate with non-disruptive method (Doubell et al. 2009). Using the same method, the roles of turbulence on formation and deformation of aggregate was presented in Chapter 2, and the difference of fluorescence intensity of aggregate in coastal water and open water was presented in Chapter 3. Since

the individual survey was conducted for a short-term period (the longest one among the data set was 18 hours) In this chapter, a long-term monitoring of aggregates is presented to explore the seasonal variation of aggregates.

4.2 Method

4.2.1 Cabled observatory; OCEANS

In order to observe a long-term change in aggregate composition, a cabled observatory system (Oshima Coastal Environmental data Acquisition Network System, herein after OCEANS, Figure 4.1) was deployed at the southeast (Habu port) of Oshima island, Tokyo, Japan (Figure 4.2). The bottom depth at the deployment location is about 20 metres. The system was mounted on a concrete block. The sensors were located ~ 3 metres above the bottom (Figure 4.1). It carries various sensors to measure pressure, current, acoustic backscatter, temperature, salinity, PAR, fluorescence, turbidity, nitrate and dissolved oxygen at a sampling rate of mostly 1 Hz (Table4.1). A plankton camera (Continuous Plankton Imaging and Classification System, herein after CPICS) is mounted on the top of OCEANS (details in 4.2.2) to record images of plankton and aggregates. Acquired data were transmitted through an optical fibre to a shore station located at Tokyo Metropolitan Government that is located at west side of Habu port and recorded in a workstation. The

power was provided from the shore station to OCEANS through the cable. In this study, temperature, salinity and pressure data were used.

Significant wave height was estimated from the root mean square of sea surface elevations (Goda and Kudaka 2007). The sea surface elevations (η_{rms}) were obtained from high accuracy pressure sensor (Fofonoff and MIllard Jr. 1983). Siginificant wave height was espressed as:

$$H_{1/3} = 4.004\eta_{rms}. \tag{4.1}$$

OCEANS did not carry shear probes that are used for conventional microstructure profilers to estimate turbulent kinetic energy dissipation rate $\varepsilon\ W\ kg^{-1}$. Assuming the lograrithmic law of the wall ε was estimate from the friction velocity (Drost et al. 2018):

$$\varepsilon = \frac{u_*^3}{kz} \tag{4.2}$$

where u_* is the friction velocity, *k* is the von Karman constant and *z* is the distance from the bottom. *k* = 0.41 and *z* = 1.2 were used. The friction velpocity was obtained from the bed shear stress (τ) and the sea water density (ρ):

$$u_* = \left(\frac{\tau}{\rho}\right)^{1/2} \tag{4.3}$$

The bed shear stress was estimated from the pure current shear stress (τ_c) and the wave related shear stress (τ_w):

$$\tau = \tau_c \left[1 + \alpha \left(\frac{\tau_w}{\tau_c + \tau_w}\right)^{\beta}\right] \tag{4.4}$$

where α=1.2 and β=3.2 (Soulsby, 1995).

Each shear stress was estimated from following equations:

$$\tau_c = \rho C_D \bar{U}^2 \tag{4.5}$$

$$\tau_w = \frac{1}{2}\rho f_w u_{w,rms}^2 \tag{4.6}$$

where C_D is the drag coefficient, $\bar{U}$ is the background velocity calculated from the velocity data obtained by Aqua Doppler Velocimeter (Vector, Nortek AS), f_w is the wave friction factor, and $u_{w,rms}$ is the orbital velocity (Wiberg et al., 2002) . The wave friction factor f_w was estimated following Swart (1974):

$$f_w = 0.00251\, exp\left[5.21\left(\frac{A}{k_s}\right)^{-0.19}\right] for\ \frac{A}{k_s} > 1.5 \tag{4.7}$$

$$f_w = 0.3\, for\ \frac{A}{k_s} > 1.57 \tag{4.8}$$

where A = $\frac{u_{w,rms}}{\omega}$ (ω is the radian frequency) and k_s is the Nikuradse roughness. k_s =0.03 was used following Drost et al. (2008).

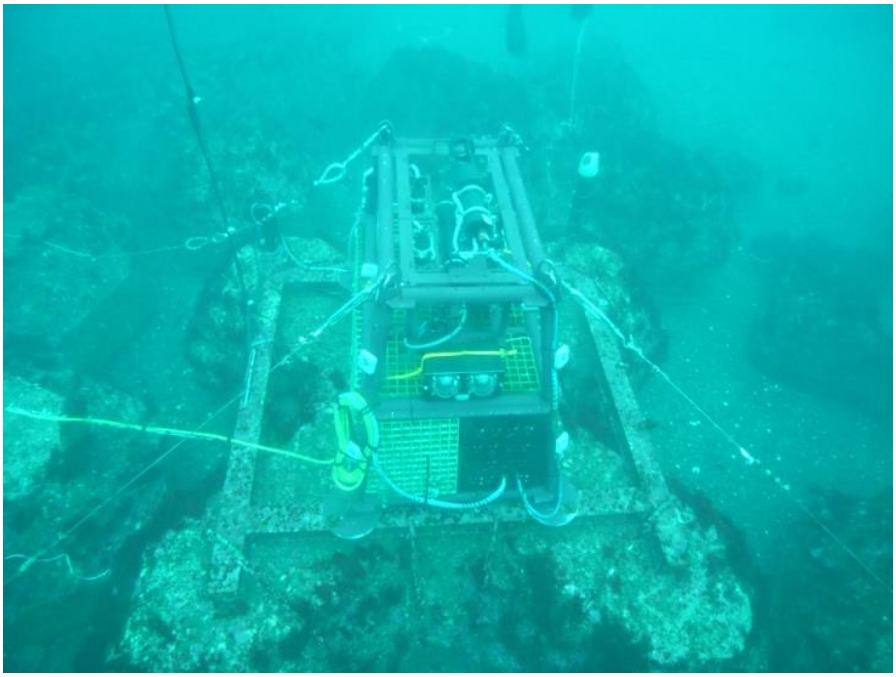

Figure 4.1 Oshima Coastal Environmental data Acquisition Network System (OCEANS) Size of OCEANS is 180 × 145 × 120 cm (width ×length ×height). The system is fixed on a block of concrete as shown in the photo.

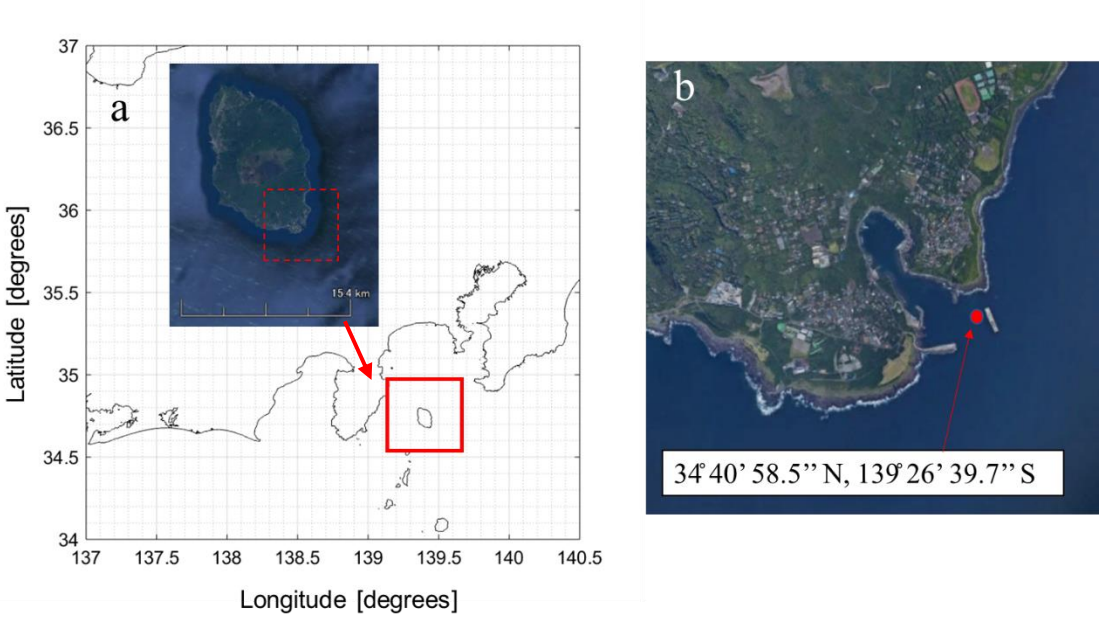

Figure 4.2 a: Location of Oshima island (red solid square), 25 km from Izu peninsula of Japan. Mount Mihara is located in the central of the island. Red dashed square indicates the location of Habu port. b:Red circle shows the location of OCEANS. No river discharge in Oshima island.

Table 4.1 OCEANS sensors sampling rate

Sensor	Sample rate
Pressure	1 Hz
Current	8 Hz
Current (Vertical)	60 secs
Acoustic backscatter (Vertical)	60 secs
PAR	1 Hz
Temperature	1 Hz
Salinity	1 Hz
Temperature (Vertical)	1 Hz
Nitrate	5 mins
DO	1 Hz
Fluorescence	1 Hz
Turbidity	1 Hz

4.2.2 Plankton camera; Continuous Plankton Imaging and Classification System (CPICS)

CPICS (Figure 4.3) was mounted on the top of OCEASNS and collected high resolution images of plankton and aggregates at sampling rate of 3Hz-7Hz (Table4.1). A field view is 11 mm ×15 mm and the focused depth is 2 mm, giving the sample volume of 330 mm^3. CPICS resolves images with a pixel resolution of 6.19 μm which is enough to identify individual plankton and aggregates. Three hundred LED light source is equipped at the opposite side of the imaging camera system. All particles in each frame are automatically detected and the region of interest (ROI) including particles is trimmed and saved. Only the images in focus were selected to be saved. Saved images of ROI are classified by an AI

based plankton classifier (LAPS Plankton Detector, LPD software). LAPS was developed by Laboratory of Plankton System (LAPS) team of the Oceanographic Institute of the University of Sao Paulo. All ROI images are classified into 51 taxa including various zooplankton, phytoplankton, aggregate, detritus and mineral grains. Through this classification process, images that classifier could not identify were classified as unknown and images that had too low resolution was filtered out as unfocused images. Aggregates were classified into two types: ones with high porosity (type A) and ones with low porosity (type B) based on the visual difference (Figure 4.4). In this study, diatom chains or detritus are excluded from aggregate taxa.

The automatic image classifier also calculate the properties of each image, such as major axis length (*MajAL*, cm), minor axis length (*MinAL*, cm), area, and equivalent spherical diameter (*ESD*, cm). Hourly averaged values of these variables were used in this study. Number spectrum as a function of *MajAL* was computed using the same method described in Chapter 2 and 3. In order to obtain accurate classification, classified images were manually validated. Since the validation was manually conducted, the available data sets were limited. In this study, two periods were compared; (1) October 2014 to January 2015 and (2) October 2015 to January 2016.

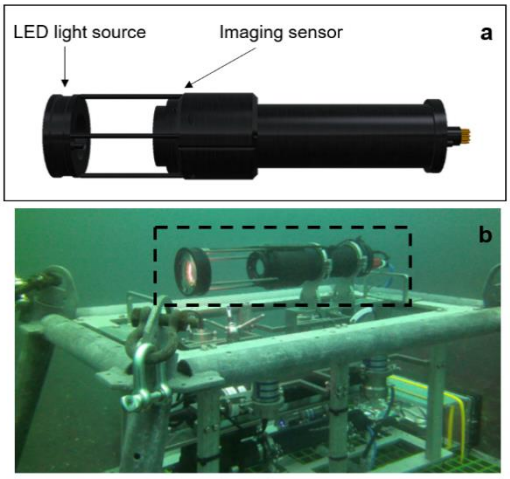

Figure 4.3Continuous Plankton Imaging and Classification System (CPICS). (a) image of CPICS (picture by Coastal Ocean Vision website). (b) underwater photo of CPICS mounted on top of OCEANS (black dashed box). The strobe is at the left end of CPICS

.

Table 4.2 Sampling rate of CPICS

	2014	2015	2016	2017
Jan		3Hz	4Hz	N/A
Feb			5Hz	
Mar			5Hz	6Hz
Apr	N/A		5Hz	6Hz
May		N/A	5Hz	6Hz
Jun			5Hz	
Jul			5Hz	N/A
Aug	3Hz		5Hz	
Sep	3Hz	4Hz		6Hz
Oct	3Hz	6Hz		6Hz
Nov	3Hz	6Hz (-Nov 12th) 4Hz (Nov 13th-)	N/A	N/A
Dec	3Hz	4Hz		

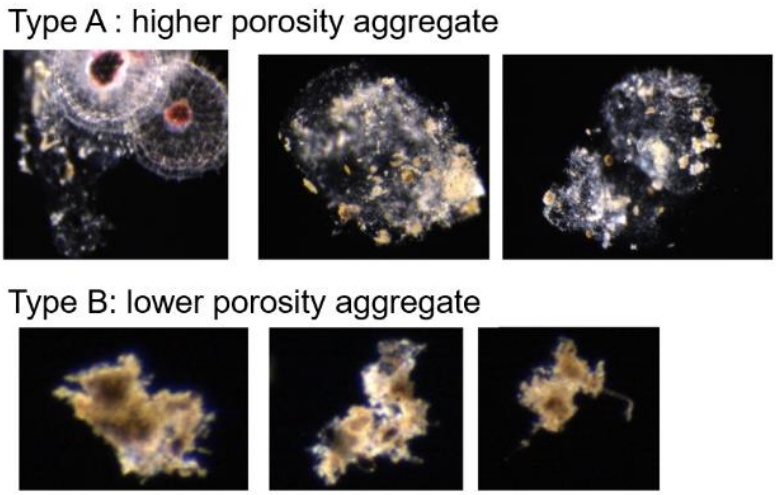

Figure 4.4 Aggregate images: Type A (top panels) and B (bottom panels). Type A aggregate contains more TEPs-like particles, which may be subjected to turbulence. Type B aggregate is denser, which is expected to have stronger bond to survive in turbulent flows. Type A aggregate shows multiple organisms, while type B shows fewer number of organisms is dominating.

4.3 Results

4.3.1 Hydrographic background

Hourly averaged temperature and salinity data were compared between period 1 and 2 (Figure 4.5). The temperature ranged between 15 and 25 ℃ for both periods, showing gradual decrease towards early January. The salinity ranged between 32 and 35 PSU, showing a temporal drop from the late October until the middle of November. Throughout the measurements, the salinity for the 2nd period appears lower than that of the 1st period. Since Oshima island is open to the Pacific Ocean, the Kuroshio may affect this area. TS-

diagram clearly shows that the 1st period exhibited open water mass type and the 2nd period showed coastal water mass type (Figure 4.6).

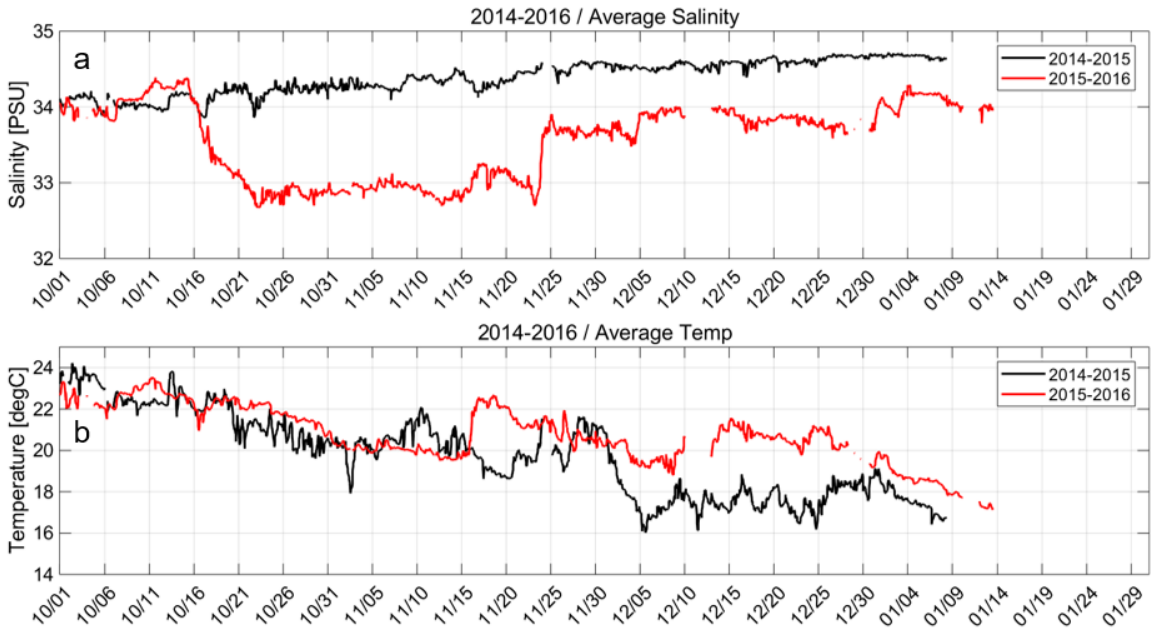

Figure 4.5 Time series of hourly average for 2014 – 2016: a) Salinity b) Temperature. Black line indicates period 1(2014 – 2015) and red line indicates period 2(2015-2016).

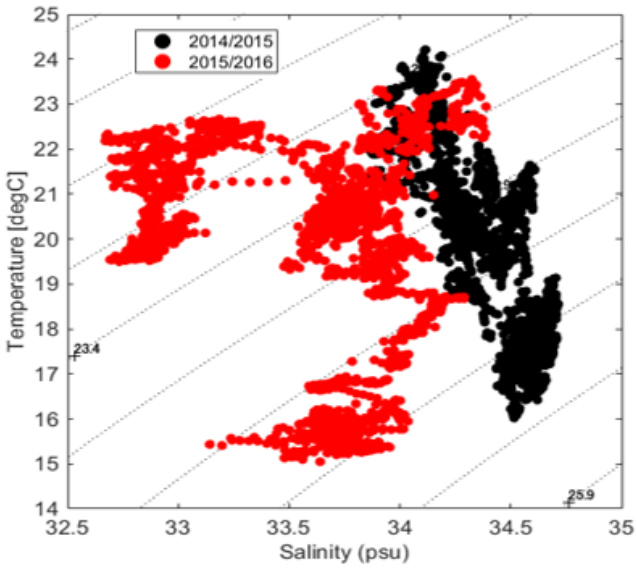

Figure 4.6 TS diagram. Black dots indicate period 1 (2014-2015) and red dots indicate period 2 (2015 – 2016). Period 2 shows lower salinity than period 1.

4.3.2 Turbulence

Turbulent kinetic energy dissipation rate ($\boldsymbol{\varepsilon}$,W kg^{-1}) remained between $o(10^{-9})$ and $o(10^{-4})$ throughout period 1 and period 2. (Figure 4.7 and Figure 4.8.a). This is commonly seen in upper ocean water column (Geyer et al. 2008; Smyth and Moum 2019). $\boldsymbol{\varepsilon}$ showed higher values when significant wave height increased (Figure 4.8.a and b). Period 2 showed higher average (1.04×10^{-6} W kg^{-1}) than period 1 (3.82×10^{-7} W kg^{-1}). Sum of multiple distributions were fitted to each distribution (Kokubu et al., 2013). Period 1 was expressed as mixture of two distributions and period2 was expressed as mixture of three distributions. Resulting fits passed Kolmogorov-Smirnov test with significant level of 5%.

4.3.3 Aggregate abundance

Number of ROI counted for period 1 and period 2 was 427,645 and 1,117,648. On average, hourly abundance of all particles was 215 L^{-1}/1hour for the 1st period while it was 541 L^{-1}/1hour for the 2nd period. Aggregate appeared more frequently during period 1; 47 % of total ROI was aggregate in period 1 and 26% in period 2. Hourly abundance of aggregate reached ~10^3 L^{-1} for both periods (Figure 4.8.c). The average hourly abundance was 60 L^{-1} for the first period and 94 L^{-1}/1hour for the second period. Relative occurrence of aggregate to other particles decreased to 26%, while hourly abundance of total particles and aggregate increased. This suggests that number of other organisms captured by CPICS increased more significantly than aggregate in period 2.

Throughout period 1 and period 2, aggregate abundance and $\boldsymbol{\varepsilon}$ did not show correlation (period 1: r^2=0.1, p<<0.01, n=1728; period 2: r^2=0.04, p<<0.01, n=2207). However, particularly during strong turbulence events (shaded area in Figure 4.8.a and Figure 4.9.a), aggregate abundance correspondingly increased with increase of $\boldsymbol{\varepsilon}$ (shaded area in Figure 4.8.c and Figure 4.9.c). Particularly first two events during period 1 showed strong correlation (1: r^2=0.50, p<<0.01, n=117; 2: r^2=0.57, p<<0.01, n=167). Since $\boldsymbol{\varepsilon}$ >10^{-6} W

kg^{-1}, the increase of aggregate abundance can be due to disaggregation by turbulence. However, the abundance of large aggregate (>1 mm) correspondingly increased (Figure 4.8.d and Figure 4.9.d). The increase of abundance simultaneously occurred over different size class and the number decreased with turbulence. Thereby, the influences of resuspension from the bottom is also negligible in increase of aggregate abundance.

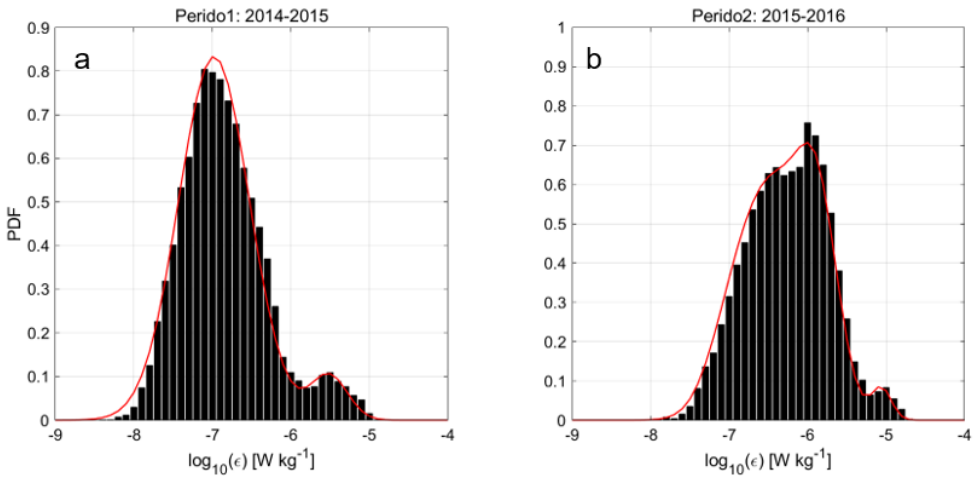

Figure 4.7 Distribution of lognormally transformed $\boldsymbol{\varepsilon}$ W kg^{-1}. Sum of multiple distributions was applied to fit the distributions. Fits are indicated with red lines. a) mixture of two populations (μ= 1.75×10^{-7} and σ^2=2.50 × 10^{-7}, μ= 3.6×10^{-6}, σ^2=1.80 × 10^{-3}). b) mixture of three populations (μ= 9.33×10^{-6} and σ^2=2.35 × 10^{-6}, μ= 2.71×10^{-7} and σ^2=1.72 × 10^{-7}, and μ= 1.59×10^{-6} and σ^2=9.41 × 10^{-7})

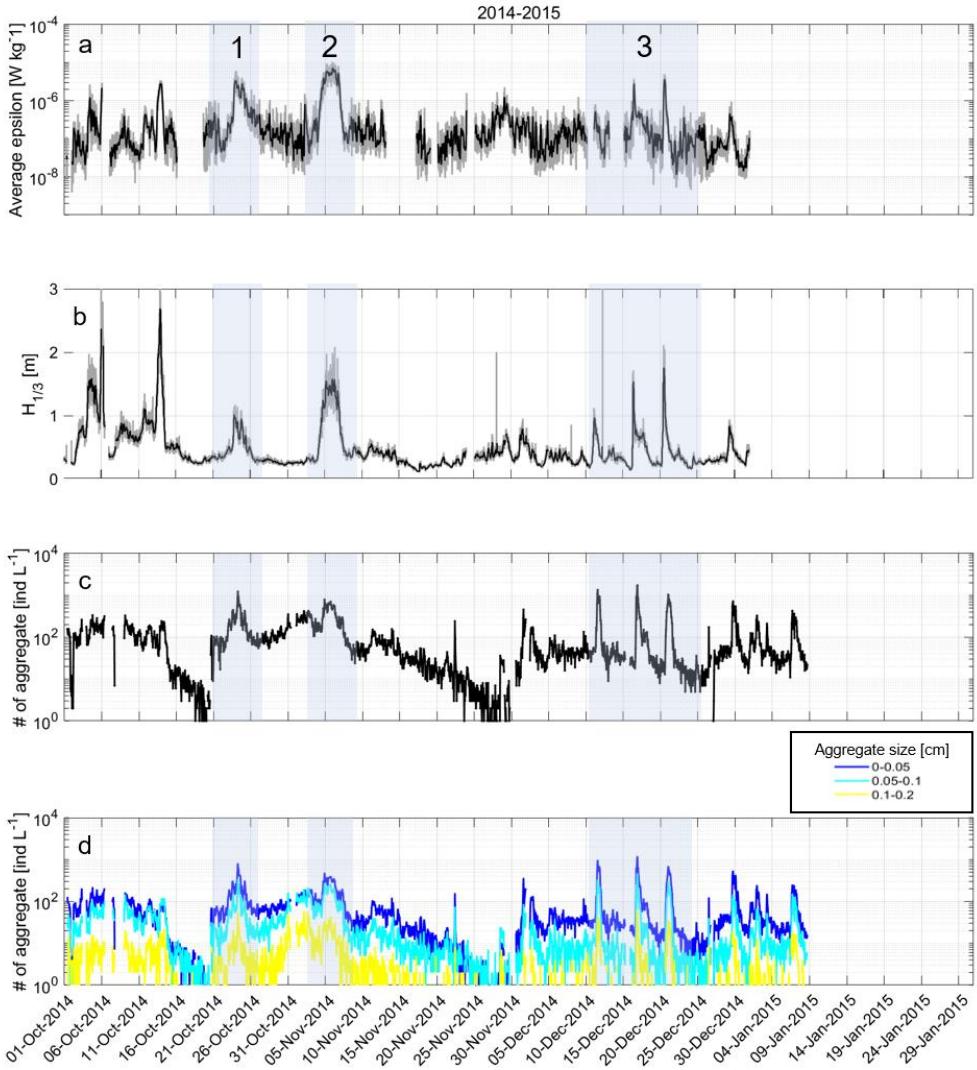

Figure 4.8 Time series of period 1: a) turbulence. Grey line shows $\boldsymbol{\varepsilon}$ estimated for 10 minutes intervals. Black line indicates moving average over 1 hour. b) Significant wave height. Grey line shows 10 minutes data and black line indicates 1 hour moving average. c) Hourly average of aggregate abundance. D) Hourly average of aggregate abundance for three size classes (blue: 0-0.05cm, cyan: 0.05-0.1 cm, and yellow: 0.1-0.2 cm)

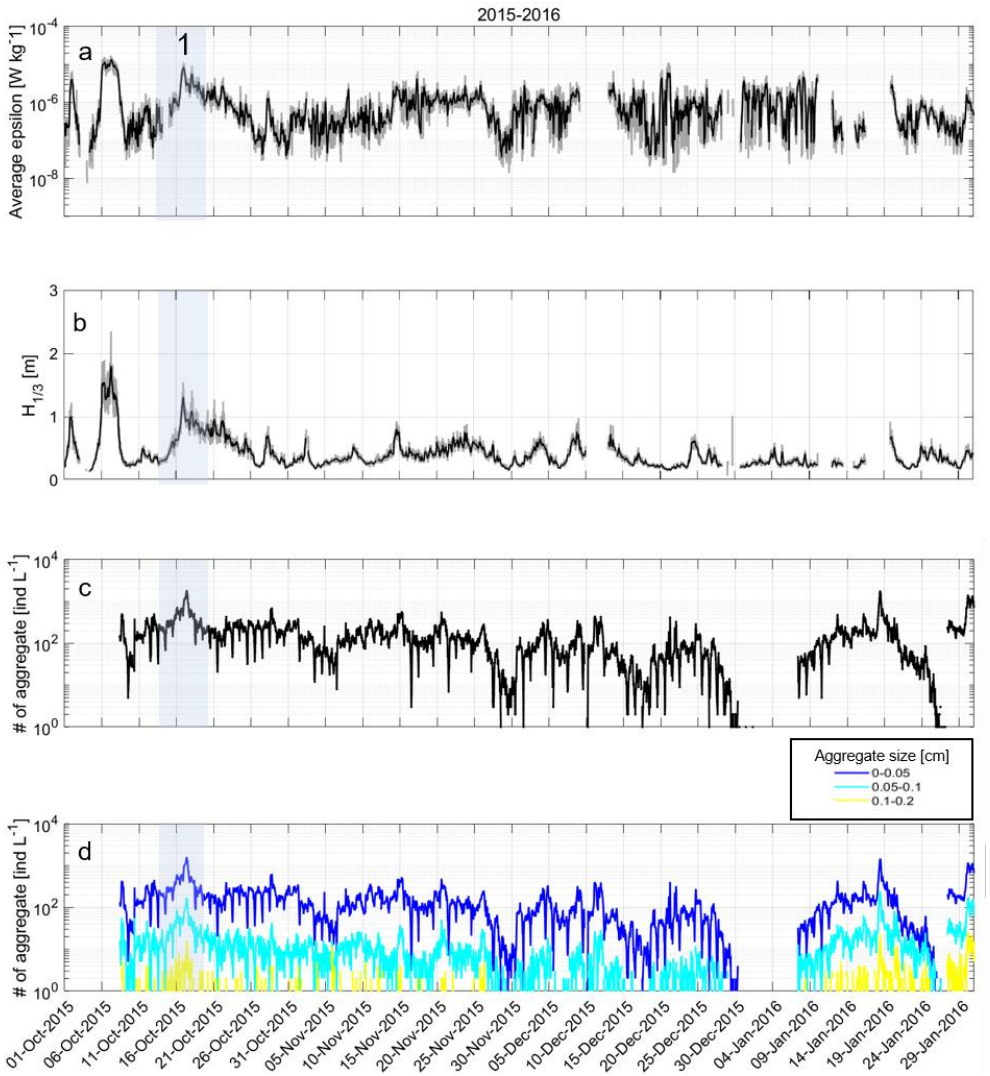

Figure 4.9 Time series of period 2: a) turbulence. Grey lines shows $\boldsymbol{\varepsilon}$ estimated for 10 minutes intervals. Black line indicates moving average over 1 hour. b) Significant wave height. Grey line shows 10 minutes data and black line indicates 1 hour moving average. c) Hourly average of aggregate abundance. D) Hourly average of aggregate abundance for three size classes (blue: 0-0.05cm, cyan: 0.05-0.1 cm, and yellow: 0.1-0.2 cm)

4.3.4 Size distribution of aggregate

Normalised number of aggregates over 12 size classes is shown in Figure 4.10 to explore the aggregate abundance with finer size scale. The most abundant size class of daily size distribution was 0.03 – 0.04 cm for the 1st period and 0.01-0.02 cm for the 2nd period. During the 1st period, 33% of total aggregate was larger than 0.05 cm. This size corresponds to marine snow (Simon et al. 2002). On the other hand, only 4 % of total aggregate was larger than 0.05 cm in the 2nd period. Large aggregate (> 0.1 cm) appeared more frequently in the 1st period; 4% appeared in the 1st period but only 0.5% appeared in the 2nd period. This is also seen in Figure 4.8.d and Figure 4.9.d. These results suggest that open water aggregates are relatively larger than coastal water aggregates, since the 1st period showed open water mass type and the 2nd period exhibited coastal water mass type (Figure 4.5 and Figure 4.6).

Figure 4.11 shows daily ratio of type A and B; type A is consisting of more Transparent Exopolymer Particles (TEPs) and type B contains less TEPs. The concentration of TEPs inside aggregate changes the strength of aggregate bound (Fettweis et al. 2014). Type A with more TEPs likely survive the disaggregation process.

Throughout the observed periods, about 50% of aggregates was type A during the1st period, on the other hand it was 32% during the 2nd period. Seasonal variation was

different for each time period. Type A was dominating in October and November during the 1st period, and type B became dominating aggregate in December. Conversely, type B was more abundant in October and November during the 2nd period, and type A became dominating aggregate in December. Large aggregate became more abundant (Figure 4.8) when type A was dominant (Figure 4.10), showing that type A aggregate was relatively larger. This is consistent with previous study that showed positive correlation between aggregate size and concentration of TEPs (Alldredge et al. 1998).

Previous study showed positive correlation between the concentration of transparent exopolymer particles (TEPs) and salinity (Najdek et al. 2011; Mari et al. 2012). Since the 1st period showed open water mass type having higher salinity, the concentration of TEPs was expected to be higher during the 1st period than that of the 2nd period. Thereby, more type A aggregate with higher TEPs was found during the 1st period. Since TEPs are negatively buoyant (Mari et al. 2017), the amount of TEPs inside aggregate has a significant influence on vertical flux.

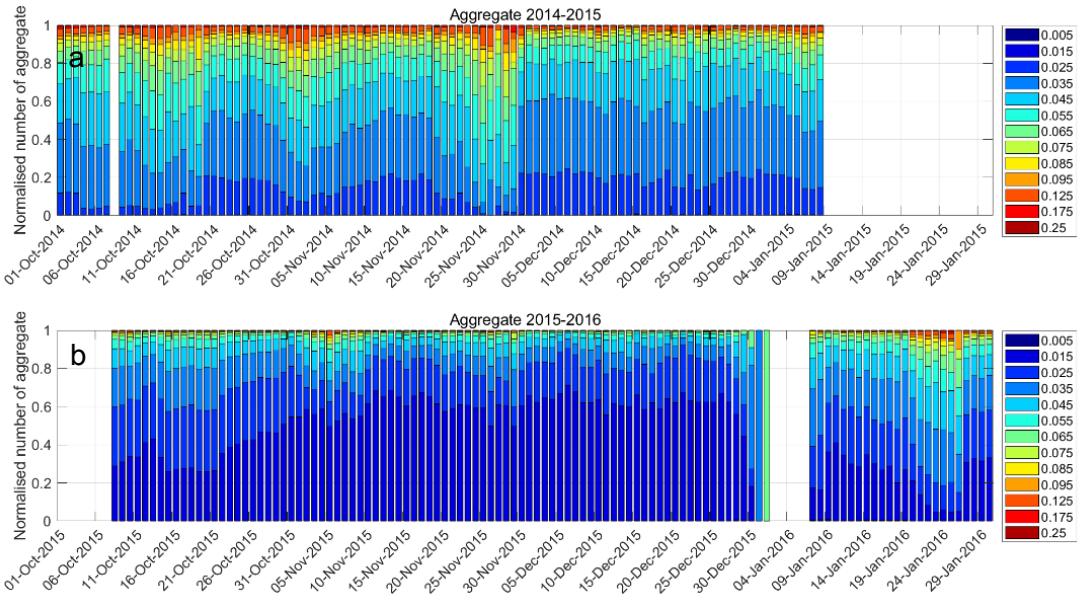

Figure 4.10 Aggregate relative abundance over 12 size classes per day: a) period 1 and b) period1.

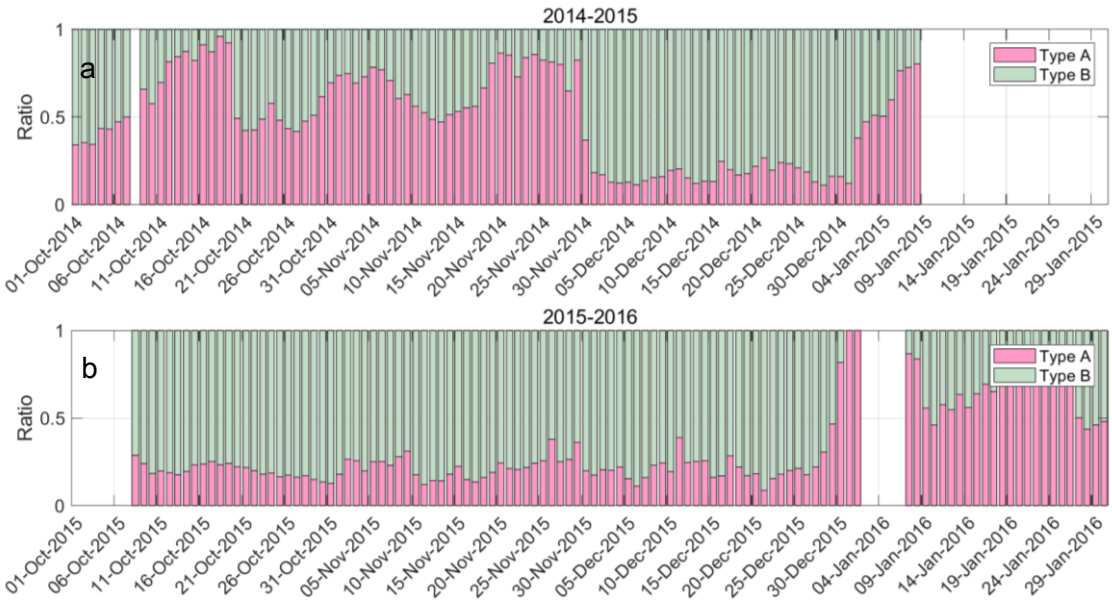

Figure 4.11 Daily ratio of aggregate type: a) period 1 and b) period 2. Type A is fluffy looking aggregate with more TEPs and Type B is denser looking aggregate with less TEPs.

4.4 Conclusion

The monitoring by OCEANS obtained long-term data sets of aggregate. Majority of aggregate seen by CPICS was small (Figure 4.8.d, Figure 4.9.d and Figure 4.10); 67% and 96% of total aggregate was smaller than 0.05 cm. Taking average of *MajAL* over time bin resulted in losing information of large aggregate and showed almost not variation in size (Appendix, Figure B). Direct comparison between $\overline{MajAL}$ and $\boldsymbol{\varepsilon}$ did not show correlation. Hourly abundance of aggregate, however, showed increase with turbulence (Figure 4.8 and Figure 4.9). Relatively strong correlation between aggregate abundance and turbulence during strong turbulence event. Disaggregation process can be enhanced under strong turbulence, $\varepsilon > 10^{-6}$ W kg $^{-1}$.Turbulence can destroy large aggregate into smaller ones and result in higher abundance. In such a case, abundance of large aggregate is expected to decrease before abundance of small aggregate increase. Figure 4.8.d showed almost no time lag between abundance of small aggregate and large aggregate. They rather increased simultaneously. This suggests that increase of aggregate abundance can be a result of resuspension. Clear evidence of aggregation or disaggregation was not found from direct comparison of aggregate size, abundance and turbulence. However, number spectra (Figure 4.12) exhibited nearly linear slopes for both 1st and 2nd period, -4.62 and -4.87 respectively. Steep slopes (~ 4) suggests that majority of aggregate measured by CPICS is

exposed to disaggregation process. However, *nVd* spectra showed that the mode remained at same size scale over different turbulence level (Figure 4.13). This result implies that the other physical and biological mechanisms also control break-up of aggregate. Since the data was continuously obtained at 3 metres above seabed, the influences of turbulence on aggregate must be different from water column, as shown in Chapter 2. Further investigation is required to clarify the roles of turbulence on aggregate at the bottom boundary layer.

Difference between period 1 and period 2 suggested features of open water type and coastal water type aggregate. Relatively large type A (more TEPs) aggregate more frequently appeared during period 1 (open water type).

However, Chapter 3 data obtained from a series of vertical profiles showed that coastal aggregates were larger than aggregate in open water. This can be due to difference in the amount of source of aggregate. Data in Chapter 3 was obtained from different location; Tokyo Bay, Otsuchi Bay, and Lake Biwa. Turbidity and fluorescence were higher in such locations than Oshima. Also, there is a significant difference mixing condition for the data obtained from OCEANS. Aggregation and disaggregation process were found in water column (Appendix, Figure A), however, disaggregation was suggested to be prominent in

this section (Figure 4.12). The process aggregate undergoes is different between water column and nears the bottom.

Data from OCEANS showed difference between aggregate in open water type and coastal water type. Seasonal variation throughout a year or interactions between different organisms have not been explored. Since CPICS obtained photos of other organisms, comparison between abundance of aggregate and other organisms is expected to develop better understanding of ecosystems.

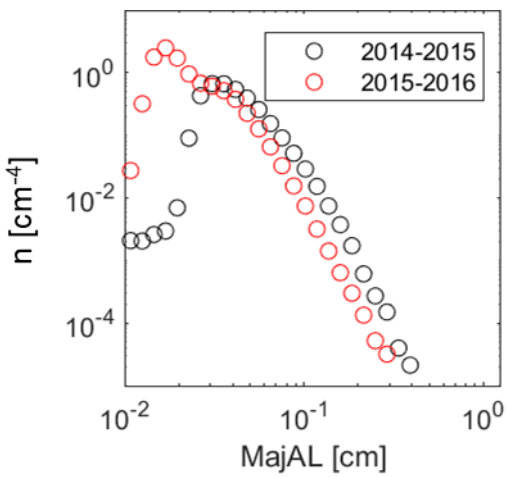

Figure 4.12 Aggregate number spectra as a function of *MajAL*. Black circles indicate 1st period and red circles indicate 2nd period. One sloe was fitted to each spectra (period 1 : -4.62 and period 2: -4.87). Steep slopes suggest that aggregate mostly undergoes disaggregation process.

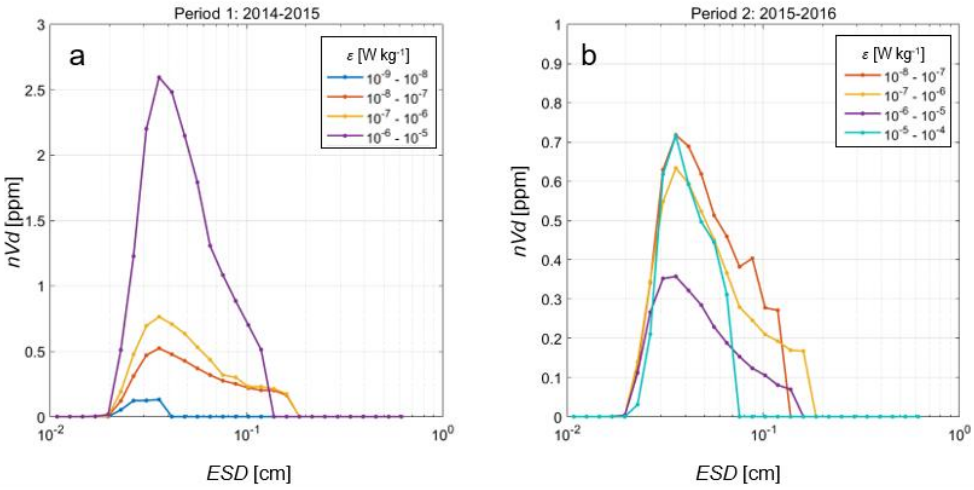

Figure 4.13 *nVd* spectra as a function of equivalent spherical diameter (*ESD*,cm) for 5 different level of $\boldsymbol{\varepsilon}$: a) period 1. Mode remained at almost same size (0.03 cm for $10^{-9}<\boldsymbol{\varepsilon}<10^{-8}$ and 0.035 cm for other orders of $\boldsymbol{\varepsilon}$). Number of samples was not sufficient to describe *nVd* for $10^{-5}<\boldsymbol{\varepsilon}<10^{-4}$. b) mode remained at same size (0.035 cm for all orders of $\boldsymbol{\varepsilon}$). Number of samples was not sufficient to describe *nVd* for $10^{-9}<\boldsymbol{\varepsilon}<10^{-8}$. The same size of mode for over different orders of $\boldsymbol{\varepsilon}$ suggests that the influences of turbulence on aggregate may be small or other physical and biological influences are prominent.

Chapter 5. Influences of different measuring methods on aggregate observations

5.1 Introduction

The studies of aggregates have been conducted by laboratory experiments, theoretical studies and *in-situ* observations. Aggregates collected in field or cultured aggregates are used for laboratory experiments (Alldredge 1998; Prairie et al. 2013). Idealised particles or sediment-rich particles are used in theoretical studies (Babler et al. 2015; Winterwerp 2002). Collection of aggregates in field may destroy aggregates during the collection and the biological and chemical features may be changed over time (Engel 2000). Cultured aggregates tend to be heavier than naturally existing aggregates (Prairie et al. 2013). Furthermore, evenly sized idealised particles and sediment-rich aggregate are stronger and heavier than phytoplankton dominating aggregate. Thereby, *in-situ* observations that measures aggregate in natural environment is necessary and numerous observation methods using optical sensors have been introduced. Holographic camera (de Jong et al. 2010) and Video Plankton Recorder (Gallager et al. 2004) can record images of plankton and aggregates in vertically and horizontal direction. However, the housing frames that hold the imaging sensors may destroy fragile aggregates. Particle sizer, such as LISST-100X, have also been used to measure aggregates in the bottom boundary layers (Safak et

al. 2013; Mikkelsen et al. 2006; Bochdansky et al. 2016). Since the instrument is fixed on a sea floor, the system provides a time series data set at a given depth but not vertical distribution of aggregate. In Chapter 2 and 3, vertical measurements of aggregate were presented. The measurements were conducted from a free-fall vertical microstructure profiler and successfully recorded aggregates with non-disruptive method. In this Chapter, two different deployment methods, a tethered deployment and a free-fall deployment, are investigated to evaluate the influences of deployment methods on aggregate measurements.

5.2 Method

An experiment was conducted at the southeast of Oshima, Tokyo, Japan (Figure 5.1). DSL camera mounted on TurboMAP-L (Chapter2, 2.2) corrected aggregate images in a the free-fall mode. Two types of holographic imaging system were deployed from a tethered mode deployment. One set of the holography system is Microstructure Holographic systems (MSS-HOLO) developed by Prof. Nimmo-Smith (Plymouth University). The other set is a digital holographic imaging system (LISST-HOLO) manufactured by Sequoia. RINKO Profiler (JEF Advantech) that measured conductivity, temperature, pressure, chlorophyll, turbidity and oxygen was mounted on each frame of the MSS-HOLO system and the LISST-HOLO system. The experiment persisted roughly 15 hours

during night-time. Ten sets of 3 consecutive deployments (DSL camera, MSS-HOLO and LISST HOLO) were conducted (Table 5.1). Although there was 30 minutes between deployment of each system, three systems measured same water mass (Figure 5.2).

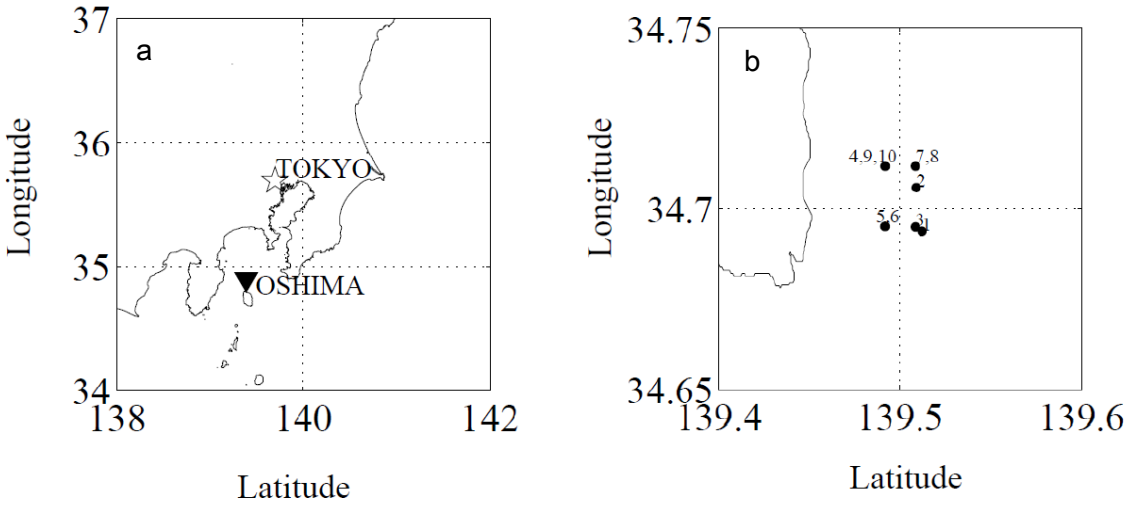

Figure 5.1 Observation site. (a) Location of Oshima island (b) locations of measurements.

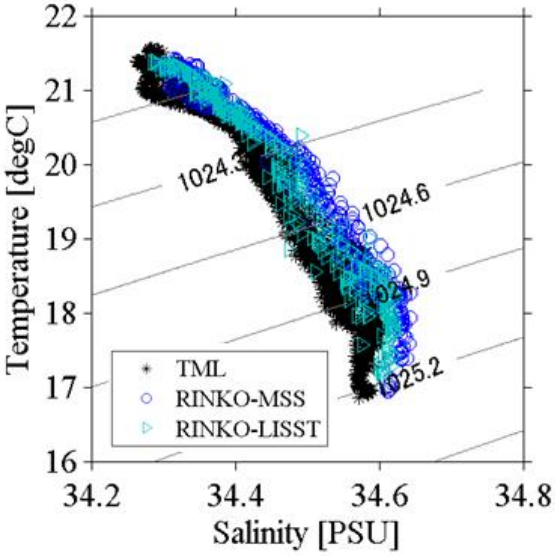

Figure 5.2 TS diagrams. Black dots indicate DSL camera with TurboMAP-L, blue circles indicate RINKO profiler with MSS-HOLO and cyan triangles indicate RINKO profiler with LISST HOLO.

Table 5.1Observation details

#	Time	Longitude	Latitude	Maximum Depth [m]			Image number		
				MSS-HOLO	LISST-HOLO	DSL (TML)	MSS-HOLO	LISST-HOLO	DSL
1	18:16	34.6937	139.5121	48.8	No Data	No Data	1858	66	No Data
2	19:49	34.7058	139.5089	39.8	No Data	51.6	1169	88	647
3	21:21	34.6949	139.5084	46.5	50.6	53	2796	95	626
4	22:49	34.7117	139.4916	36.8	51.5	53.1	1077	66	647
5	0:43	34.695	139.4915	51.7	28.7	57.9	2047	97	684
6	1:58	34.6949	139.4916	51.4	52.1	54.7	1811	84	726
7	3:16	34.7117	139.5084	51.5	51.1	59.8	1738	83	683
8	4:47	34.7117	139.5083	49.9	No Data	No Data	1331	51	No Data
9	6:20	34.7118	139.4917	52	50.4	No Data	974	65	No Data
10	7:47	34.7117	139.4917	48.3	No Data	No Data	2064	133	No Data

5.2.1 Holography deployment

MSS-HOLO (Plymouth University, Figure 5.3.a) and LISST-HOLO (Sequoia Scientific Inc., Figure 5.3.b) were lowered by a tethered cable at 0.1 m s^{-1} and 1 m s^{-1}, respectively. MSS-HOLO recorded images at 5 Hz with a field view of 0.52 ×0.35 cm^2 and the depth of image was 2.5 cm; thus, the sampling volume is 0.455 cm^3. The pixel resolution is 3.4 µm and particles larger than 11.5 µm can be identified. Images were transmitted and recorded on a shipboard computer, thereby real time monitoring was available. LISST-HOLO recorded images at 1 Hz and images were stored in an internal memory stick. A field view of LISST-HOLO was 0.70 ×0.53 cm and the depth of image was 2.9 cm; thus the sampling volume is 1.08 cm^3. A pixel resolution is 4.4 µm and particles larger than 25 µm can be identified. Although both systems are designed to measure the environmental physical parameters, such as depth, temperature and conductivity, LISST-HOLO had a technical trouble and did not record the depth. The depth was estimated from RINKO-profiler mounted on the same frame, by interpreting temperature data of LISST-HOLO and RINKO-profiler. RINKO data were not available for the first two deployments and deployment 10. Temperature data for deployment 8 from LISST HOLO were also not available; thus no depth data were obtained.

5.2.2 Data processing of holograms

Holographic system captures the interference patterns that are created when particles pass the sampling volume; particles diffract a coherent laser beam and the diffracted laser beams and collimated laser beams create interference patterns. The patterns are recorded as holograms on the Charge- Coupled Device (CCD) image sensor at the other side of emitting laser beam (Graham and Nimmo Smith 2010). The interference patterns contain phase and amplitude which indicate the distance from the camera and the size of the particle. Recorded holograms are digitally reconstructed to bring measured objects into focus using the software HOLO Batch (Sequoia Scientific Inc.) that runs on MATLAB (Mathworks Inc.). A simplification of convolution approach is used for reconstruction (Graham and Nimmo Smith 2010; Owen and Zozulya 2000), expanding 2 dimensional holograms into 3 dimensional images. Images are vertically sliced for every 0.0195 cm towards z-axis to obtain distance of each particle from the imaging camera. Finally, black and white images with particles in focus, images that indicates the distance of particles from the camera by colour were generated in 2Ds (Figure 5.4b). During the reconstruction process, particle properties are calculated. In-focus particles are estimated as ellipses and particle properties are automatically extracted using MATLAB built in function *regionprops*; major axis length (*MajAL*), convex area (area including internal holes; A_c),

area (area without internal holes; A) were used in this study. A ratio between convex area and area, $R = \frac{A}{A_c}$, was used to separate aggregate from others; R of porous particles are ~1 and solid particles are ~0. Since aggregate is commonly porous particles (Silver 2015), particles with R>0.5 were identified as aggregates in this study. Number spectra was constructed for holographic systems and DSL, following the method described in Chapter 2.

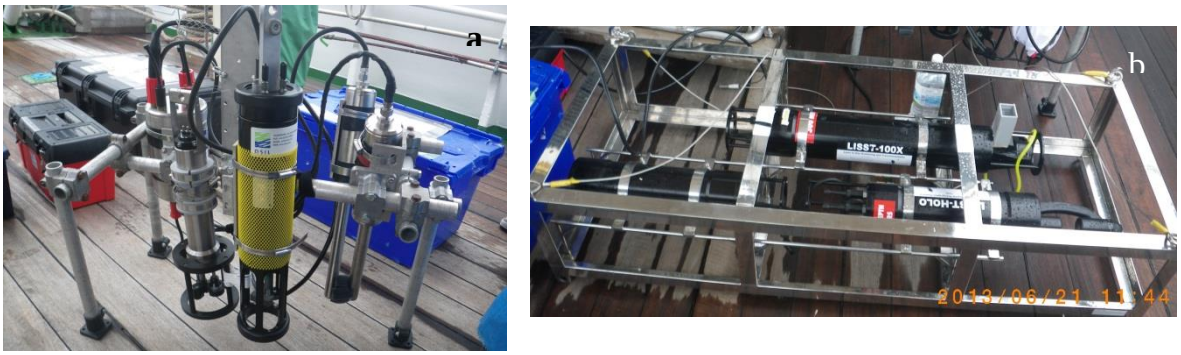

Figure 5.3 Holographic systems. (a) Microstructure holography (MSS-HOLO). (b) LISST-HOLO.

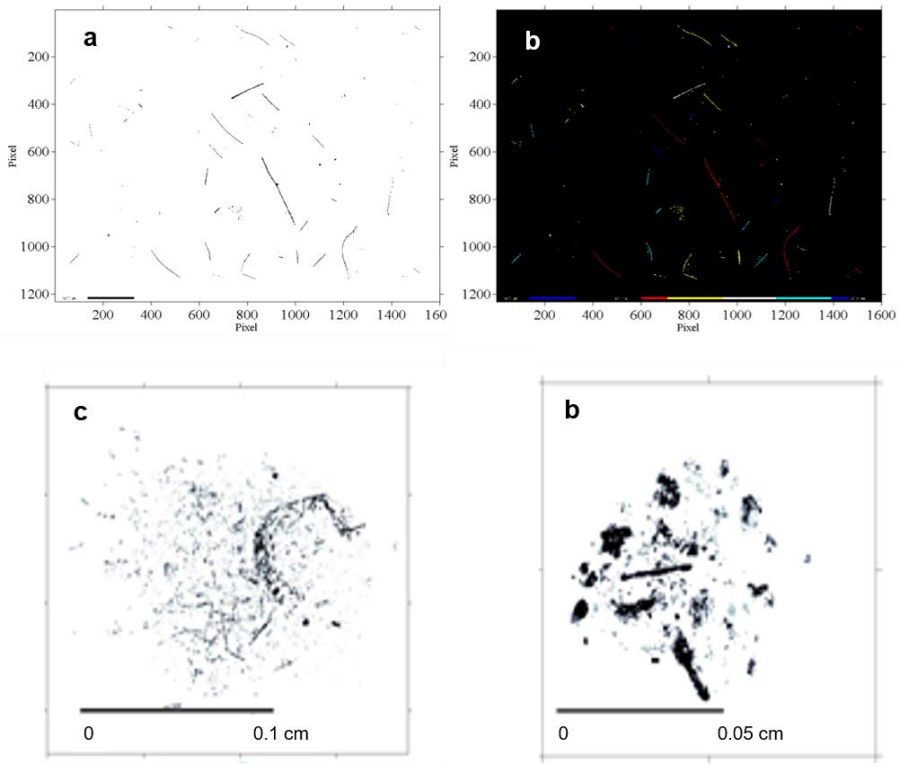

Figure 5.4Reconstructed holograms. (a) Example of montage image of reconstructed holograms. (b) Example of image indicating distance in colour. (c) Example of aggregate image obtained from MSS-HOLO (d) Aggregate obtained by LISST-HOLO

5.2.3 RINKO profiler

RINKO profiler (JFE Advantech Co., Ltd.) was mounted on both MSS-HOLO system and LISST-HOLO system to obtain hydrographic data in better resolution. RINKO profiler collected following data at 2.5-5Hz; pressure, fluorescence, turbidity, conductivity, and dissolved oxygen (Table 5.2). A RINKO profiler was mounted on a single frame with MSS-HOLO.

Table 5.2 RINKO Profiler specification

Parameters	Range	Accuracy	Resolution	Sampling rate [Hz]
Depth [m]	0 to 600	±0.3%	0.01m	5
Temperature [degC]	-3 to 45	±0.01	0.001	5
Conductivity [mS/cm]	2 to 70	±0.01	0.001	5
Salinity [PSU]	2 to 42	±0.01	0.001	5
Dissolved Oxygen [mg/L]	0 to 20	±2%	0.001	2.5
Chlorophyll [ppb]	0 to 400	±1%	0.01	5
Turbidity [FTU]	0 to 1	±0.3	0.03	5

5.3 Results

5.3.1 Horizontal structures

The observed temperature ranged approximately between 16 and 21 ℃ and the surface temperature remained ~ 21 ℃ during the experiment. A surface mixed layer extended down to ~30 metres until midnight and pushed upwards, up to 20 metres, around 6 a.m. Chlorophyll-*a* maxima appeared between 10 and 30 meters where a thermocline was observed (Figure 5.5 a, b,c). A total number of aggregates over 1 metre was divided by

sampling volume to obtain aggregate abundance (# of aggregates cm^{-3}). Consistently to the depth where chlorophyll-*a* maxima appeared, according to MSS-HOLO and DSL camera showed high abundance of aggregate (Figure 5.5 d and e) that is consistent with high values of chlorophyll-*a* obtained by RINKO Profiler (Figure 5.5c). LISST-HOLO data were too course in spatial resolution and the pattern of spatial distribution is vague in comparison with MSS Holo data (Figure 5.5 d and e). Aggregate abundance ranged between 0.092 – 9.6 cm^{-3} with MSS-HOLO and 0.24 – 3.2 cm^{-3} for DSL camera. Aggregate abundance measured by MSS-HOLO was about 3 times higher than that of aggregate abundance measured by DSL camera.

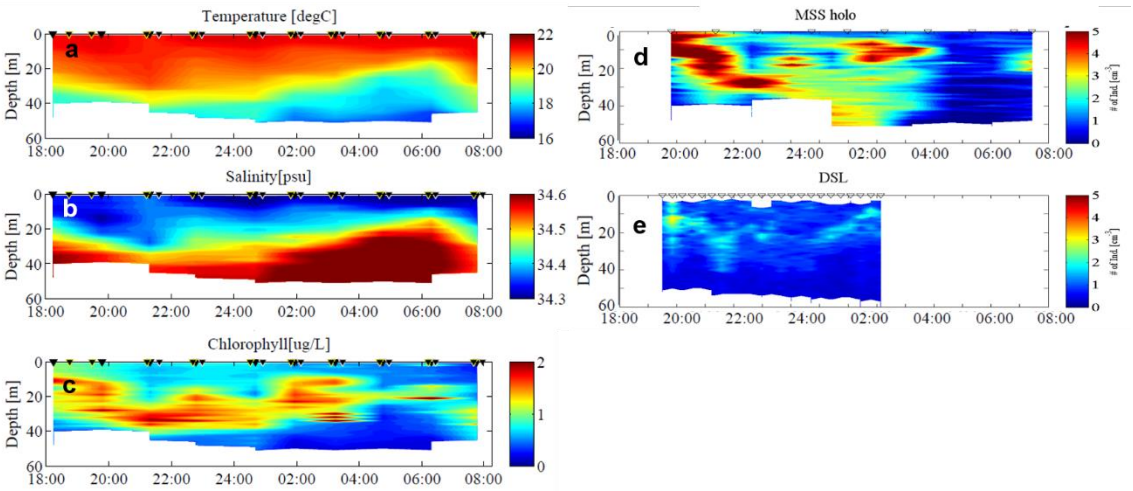

Figure 5.5 Horizontal distribution of (a) temperature (b) salinity (c) chlorophyll-a (d) aggregate abundance measured by MSS-HOLO and (e) aggregate abundance measured by DSL camera

5.3.2 Size distribution

Number spectra were constructed for each instrument (n_{MSS}, n_{LISST}, n_{DSL}, cm^{-4}) to compare size distribution obtained by different instruments (Figure 5.6). Both n_{MSS} and n_{LISST} showed higher abundance than that of n_{DSL}. Namely, more aggregates were observed by holographic systems than that of DSL. Slope 1 was -1.62 (MSS-HOLO), -1.53 (LISST-HOLO) and -2.02 (DSL). Slope 2 was -3.31, -3.65 and -4.39 respectively. The fitted slopes for the holographic systems were less steep than that of DSL. The intersection between Slope 1 and Slope 2 appeared at 0.10 cm (MSS-HOLO), 0.043 cm (LISST-HOLO) and 0.24 cm (DSL), respectively. According to the TS-diagrams obtained from these instruments (Figure 5.2) showed the same water mass type; however, both particle abundance (Figure 5.5) and number spectra (Figure 5.6) showed higher abundance in holographic measurement. Furthermore, the intersections of Slop 1 and Slope 2 for holographic systems appeared much smaller scale than that of DSL system.

Aggregation is more enhanced over size class where slope 1 was fitted and disaggregation is strongly enhanced in a slope 2 range. The intersection between Slope 1 and Slope 2 occurs close to the Kolmogorov scale (L_k) given by $\left(\varepsilon/\nu^3\right)^{-\frac{1}{4}}$, where ν is kinematic viscosity and ε is turbulent kinetic energy (TKE) dissipation rate according to

the results presented in Chapter 2 . Assuming the intersections of number spectrum ~ L_k, TKE dissipation rate that each instrument experienced may be estimated.

A cruise average turbulent kinetic energy dissipation rate (ε, W kg^{-1}) is estimated from TurboMAP-L microstructure data during the experiment. The average dissipation rate is ~3.7×10^{-8} W kg^{-1} that is L_k = ~ 0.23 cm. This is almost same size scale of the intersection of n_{DSL}, 0.24 cm.

The intersection of n_{MSS} appeared at 0.1 cm that is L_k when ε= o(10^{-6}) W kg^{-1}. Even smaller intersection of n_{LISST} (0.043 cm) is between L_k at ε= o(10^{-5}) W kg^{-1} and L_k at ε= o(10^{-4}) W kg^{-1} (0.056 cm and 0.031 cm). These facts suggest that aggregates observed by the holographic systems experienced much stronger turbulence than that of DSL system. The stronger turbulence on holographic systems may cause the higher aggregate abundance in holographic systems (Figure 5.5) and the intersection on number spectra appeared at a smaller scale (Figure 5.6).

Since the deployment of DSL camera (TurboMAP-L) was in a free-fall mode, the instrument did not disturb the surrounding water column (Figure 5.7.a and d). On the other hand, the holographic systems were mounted on a tethered cable system that could cause

upward/down motions during deployment. Such motions reached as high as 1 m s^{-1} (Figure 5.7.b,c,e and f). MSS-HOLO reached sinking velocity $\pm$ 0.5 m s^{-1} and LISST-HOLO reached $\pm$ 1 m s^{-1}. Extra turbulence introduced due to upward motion might have caused destruction of aggregates in the holographic systems.

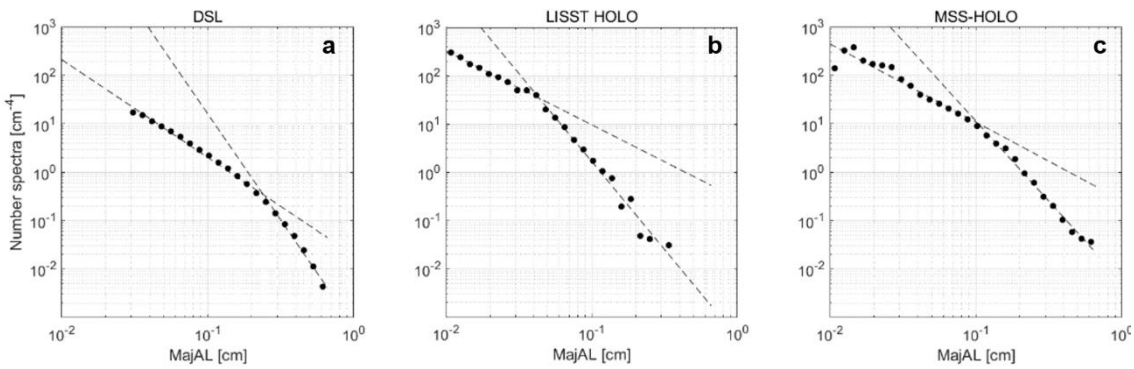

Figure 5.6 Number spectra of aggregateas a function of *MajAL*:a) DSL camera ,b) LISST-HOLO and c) MSS-HOLO

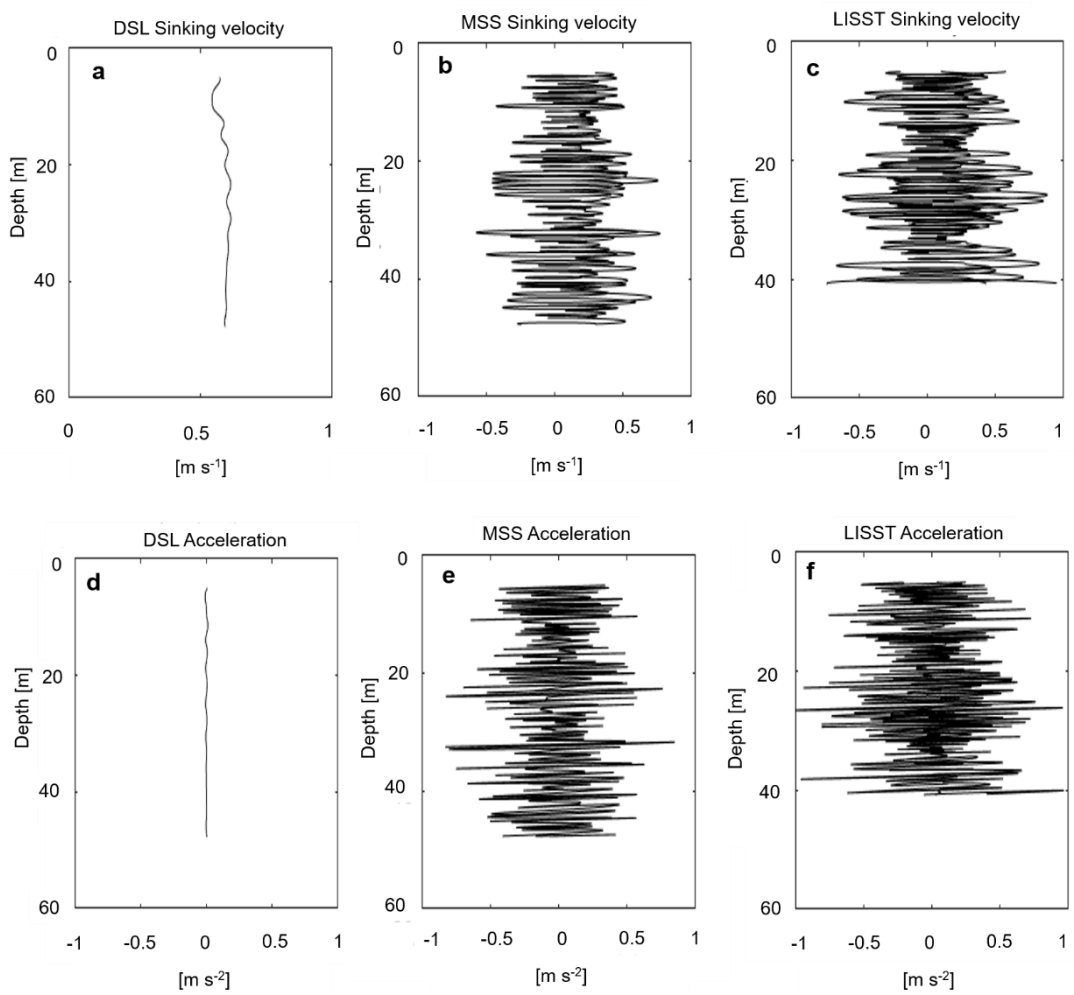

Figure 5.7 Sinking velocity and acceleration. (a and d) DSL camera (b and e) MSS-HOLO (c and f) LISST-HOLO

Figure 5.7

5.4 Conclusion

The holographic systems captured clear images of aggregate in water column (Figure 5.4.c and d), showing that the holographic systems are potentially powerful tools that allow us to identify the detail of individual aggregate in a water column. Throughout the observations, consistent results between the DSL camera system and the holographic

systems were expected, since there were measuring the same water mass (Figure 5.1). However, particle abundances (Figure 5.5) and number spectra (Figure 5.6) showed significant differences in abundance and size distributions. Estimated ε from the intersections of number spectra (Figure 5.6) suggested that aggregates observed by holography systems experienced much stronger turbulence (epsilon for MSS and Holo) than the turbulence intensity ~o (10^{-8}) W kg^{-1} observed by TurboMAP-L. This result suggested that aggregates observed by the holographic systems were disturbed by the instrument itself and the supporting flame. As shown in Figure 5.7, sinking velocity showed strong upward and downward motions. Since the holographic systems were deployed by tethered cables, the motions of the vessel had direct influence on the instrument motion. In order to avoid artificially created high turbulence intensity, the holographic systems must be deployed with a disturbance free mode. Since a free-fall mode of TurboMAP-L does not cause such disturbance, a similar free-fall deployment method should be developed.

Chapter 6. Chapter 6 Conclusions and future works

The DSL camera successfully captured the images of aggregate in a water column without destroying aggregates. Accumulating image data collected over 10 campaigns at multiple locations demonstrated the roles of turbulence on formation and destruction of aggregates in a water column away from the surface and the bottom boundary layer. Figure 2.6 showed that both aggregation and disaggregation process can occur at any level of turbulence. As coagulation theory has suggested that particles keep experiencing aggregation and disaggregation processes (Jackson 1990; Li et al. 2004). Although aggregation and disaggregation can occur at any level of turbulence, Figure 2.2.a showed aggregation process is prominently driven by turbulence up to $\varepsilon = 10^{-6}$ W kg^{-1}. Above this scale, turbulence promotes disaggregation. Since ε is less than 10^{-6} W kg^{-1} in the majority of water column (Geyer et al. 2008; Smyth and Moum 2019), turbulence mainly drives aggregation process in most fraction of the world ocean. In addition to turbulence, total volume concentration of aggregate also enhances aggregation (Figure 2.2.b). Morphological change in aggregates due to turbulence was observed (Figure 2.4.a). Since sinking speed of aggregate increases with its size (Khelifa and Hill 2017) and elongation (Clifton et al. 2018; Ruiz et al. 2004), increased size and elongation under stronger turbulence will promote vertical flux even more. Turbulence is recognized as an important

factor that controls oceanic mixing under expecting climate change. The findings according to aggregation driven by turbulence shows turbulence is also an important key to control vertical flux of biogeochemical materials through sinking behavior of aggregates.

In Chapter 3, the comparison between open water and coastal water aggregate showed that fraction of water occupied with aggregate for open water is smaller than that of coastal water; however, the phytoplankton concentration in individual aggregate for open water is much higher than that of coastal water case (Figure 3.4.b). The Kuroshio extension which is the main observation location in open water for this study is known as an oligotrophic environment, but contradictory the Kuroshio is highly productive (Sogawa et al., 2019). The intense phytoplankton concentration in aggregate shows that aggregate is a significant contributor to support nutrient and food in open water.

A long-term monitoring of aggregates by OCEANS also showed clear difference in size and components between aggregate in coastal water and open water. In open water type, relatively larger and type A (higher TEPs) aggregate was more frequently seen than coastal water type. This is consistent with previous study that suggested positive correlation between salinity and concentration of TEPs (Najdek et al. 2011; Mari et al. 2012). Aggregate abundance increased when turbulence and significant wave height were higher (Figure 4.8 and Figrue 4.9). This can be the conbination of aggregate break-up by

turbulence and resuspention from the bottom. Relative abundance of type A aggregate (Figure 4.11) increased when abundance of aggregate increased. Since aggregate with more TEPs is lighter and sometimes even negatively buoyant (Mari et al., 2017), the increase of typeA aggregate may be due to resuspention. Although disaggregation process was suggested (Figure 4.12), clear relationship between aggregate and turbulence was not found. More data may be required to further investigate the relationship between aggregate and turbulence at the bottom boundary layer. In Chapter 2, the relationship between turbulence and forrmation and destruction of aggregate was shown. In Chapter 3, comparison between aggregate volume concentration and fluorescence showed difference between aggregate in open water and coastal water. Chapter 4 also showed the difference between open water and coastal water, and related aggregate properties. Such results were successfully obtained because the observations were conducted by non-disruptive methods; free-fall and observatory. Chapter 5 demonstrated the importance of such 'non-disruptive' methods to explore aggregate properties accurately in the fields. Cable-controlled deployments of holographic systems exhibited the instruments experienced sudden upward motions (~1 m s^{-1}) (Figure 5.7). This suggested aggregate observed by holographic systems were exposed to much stronger turbulence than aggregate observed by DSL camera which

was in free-fall (Figure 5.6). This result highlighted that it is necessary to conduct non-disruptive deployments for aggregate measurements.

6.1 Future outlooks

The observations by DSL camera successfully demonstrated the relationships between aggregate and turbulence. The importance of aggregate in open water as hotspots of phytoplankton was also shown. In order to verify the results, applying models and taking water samples are important. Particularly, chemical information such as concentration of carbon and TEPs is necessary to further understand the roles of aggregate in vertical flux and ecosystems Comparison between the observational data presented here and coagulation theory will link the theoretical studies and field data. In addition, recent LES simulations showed the relationship between turbulence and phytoplankton patchiness (Brereton et al. 2018). Combining coagulation theory and numerical works with observational data may lead further understanding on aggregate distribution in the ocean.

Chemical and biological parameters were simultaneously obtained by OCEANS. Comparing aggregate with such parameters is expected to find how aggregate respond to environmental change. In this study, data for limited duration was analysed and it was not enough to show seasonal variation. Extending the data set is expected to show the seasonal variation. Furthermore, the interactions with other organisms have not been investigated.

Since zooplankton and fish feed on aggregate (Kiøboe 2001; Larson and Shanks 1996), correlation between aggregate and other organisms can be found. Exploring the interaction of aggregate and other organisms will develop our understanding in the roles of aggregate in the ecosystems.

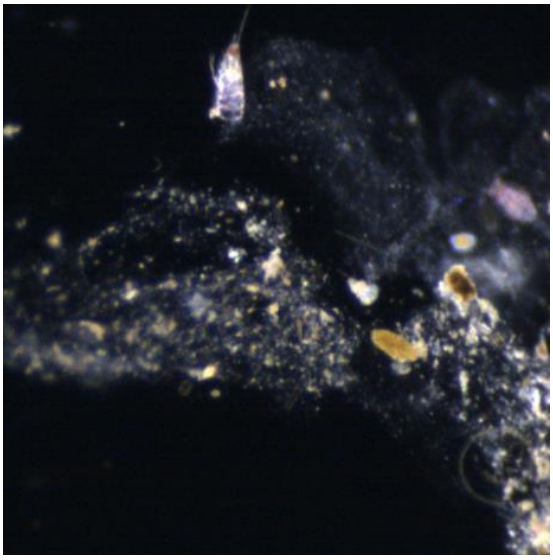

Figure 6.1 Copepod feeding on aggregate. Image was obtained by CPICS.

Appendix

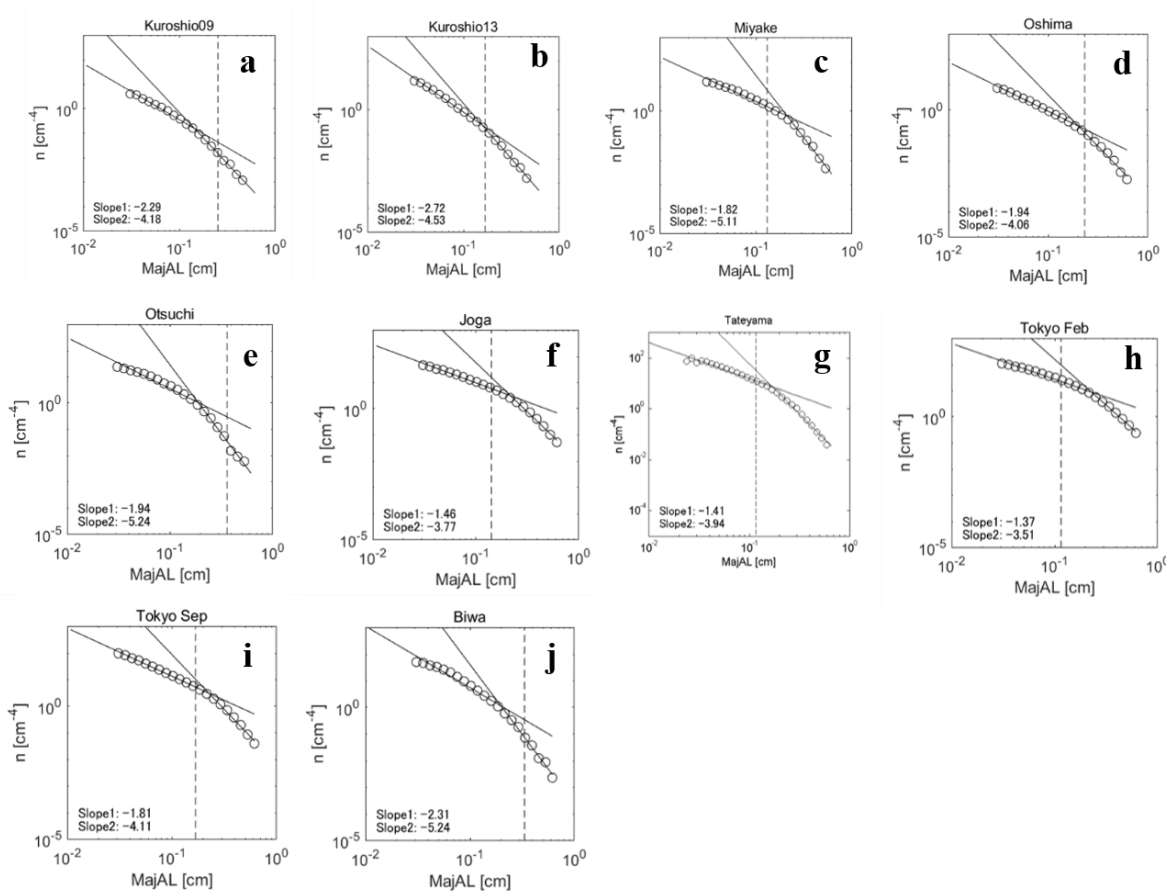

Figure A Size spectrum for each observation site. Total aggregate used is 26,791 in Kuroshio 2009, 17,526 in Kuroshio 2013, 45,004 in Otsuchi, 121,977 in Biwa, 208,716 in Joga, 42,340 in Miyake, 74,418 in Tateyama, 167,244 in Tokyo February and 196,792 in Tokyo September.

Table A Size spectrum intersections, L_k, slope 1, slope 2 and the ratio between intersection an L_k.

		Int. [cm]	L_k[cm]	Slope1	Slope2	Lk/int.
Open water	Kuroshio09	0.14	0.25	-2.29	-4.18	1.7
	Kuroshio 13	0.16	0.17	-2.72	-4.53	1.1
	Miyake	0.21	0.13	-1.82	-5.11	0.62
	Oshima	0.2	0.23	-1.94	-4.06	1.2
Coastal water	Otsuchi	0.19	0.36	-1.94	-5.24	1.9
	Joga	0.22	0.14	-1.46	-3.77	0.66
	Tateyama	0.21	0.11	-1.69	-4.11	0.52
	Tokyo Sep	0.23	0.12	-1.37	-3.51	0.51
	Tokyo Feb	0.23	0.17	-1.81	-4.11	0.75
Lake	Biwa	0.2	0.33	-2.31	-5.24	1.7

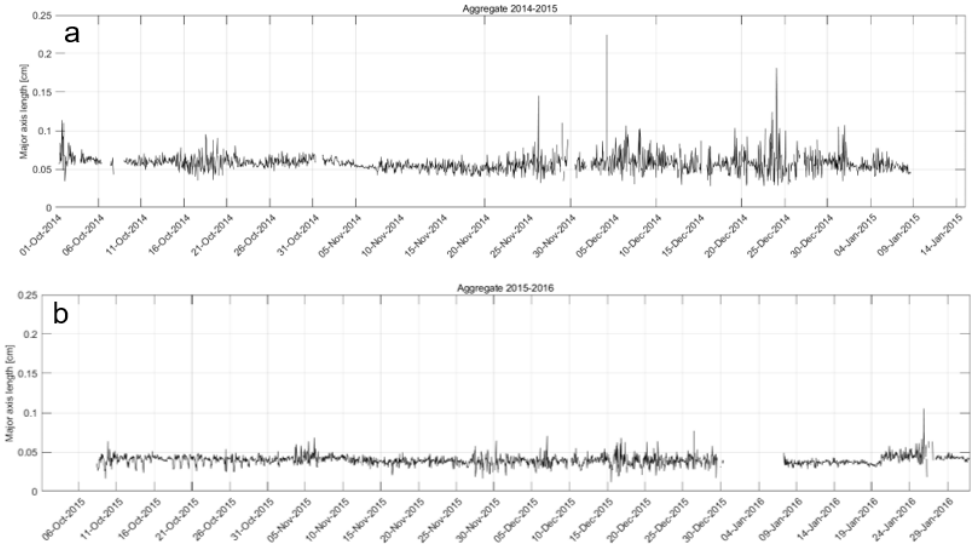

Figure B Hourly average of MajAL obtained by OCEANC (Chapter 4): a) Period 1, b) Period 2.

References

Alldredge, A. L., and C. C. Gotschalk. 1989. 'Direct observations of the mass flocculation of diatom blooms: characteristics, settling velocities and formation of diatom aggregates', *Deep Sea Research Part A, Oceanographic Research Papers*, 36: 159-71.

Alldredge, Alice L., and Chris Gotschalk. 1988. 'In situ settling behavior of marine snow", *Limnology and Oceanography*, 33: 339-35.

Alldredge, Alice L., Timothy C. Granata, Chris C. Gotschalk, and Tommy D. Dickey. 1990. 'The physical strength of marine snow and its implications for particle disaggregation in the ocean', *Limnology and Oceanography*, 35: 1415-28.

Alldredge, Alice L., Uta Passow, and H. D. Haddock. 1998. 'The characteristics and transparent exopolymer particle (TEP) content of marine snow formed from thecate dinoflagellates', *Journal of Plankton Research*, 20: 393-406.

Alldredge, Alice. 1998. 'The carbon, nitrogen and mass content of marine snow as a function of aggregate size', *Deep Sea Research Part I: Oceanographic Research Papers*, 45: 529-41.

Azam, Farooq. 1998. 'Microbial Control of Oceanic Carbon Flux: The Plot Thickens', *Science*, 280: 694-96.
Azam, Farooq, and Richard A. Long. 2001. 'Sea snow microcosms', *Nature*, 414: 495-98.

Babler, Matthaus U., Luca Biferale, Luca Brandt, Ulrike Feudel, Ksenia Guseva, Alessandra S. Lanotte, Cristian Marchioli, Francesco Picano, Gaetano Sardina, Alfredo Soldati, and Federico Toschi. 2015. 'Numerical simulations of aggregate

breakup in bounded and unbounded turbulent flows', *Journal of Fluid Mechanics*, 766: 104-28.

Bhaskar, P. V., and N.B. Bhosle. 2005. 'Microbial extracellular polymeric substances in marine biogeochemical processes', *Current Science*, 88: 45-53.

Bochdansky, Alexander B., Melissa A. Clouse, and Gerhard J. Herndl. 2016. 'Dragon kings of the deep sea: marine particles deviate markedly from the common number-size spectrum', *Scientific Reports*, 6: 22633-33.

Bowers, D. G., C. E. Binding, and K. M. Ellis. 2007. 'Satellite remote sensing of the geographical distribution of suspended particle size in an energetic shelf sea', *Estuarine, Coastal and Shelf Science*, 73: 457-66.

Braithwaite, K. M., D. G. Bowers, W. A. M. Nimmo Smith, and G. W. Graham. 2012. 'Controls on floc growth in an energetic tidal channel', *Journal of Geophysical Research: Oceans*, 117: 1-12.

Brereton, A., J. Siddons, and D. M. Lewis. 2018. 'Large-eddy simulation of subsurface phytoplankton dynamics: an optimum condition for chlorophyll patchiness induced by Langmuir circulations', *Marine Ecology Progress Series*, 593: 15-27.

Burd, A., and G. A. Jackson. 1997. 'Predicting particle coagulation and sedimentation rates for a pulsed input', *Journal of Geophysical Research: Oceans*, 102: 10545-61.

Clifton, W, R.N. Bearon, and M.A. Bees. 2018. 'Enhanced sedimentation of elongated plankton in simple flows', *Journal of Applied Mathematics*, 83: 743-66.

de Jong, J., J. P. L. C. Salazar, S. H. Woodward, L. R. Collins, and H. Meng. 2010. 'Measurement of inertial particle clustering and relative velocity statistics in isotropic turbulence using holographic imaging', *International Journal of Multiphase Flow*, 36: 324-32.

Doubell, Mark J., Hidekatsu Yamazaki, Hua Li, and Yusaku Kokubu. 2009. 'An advanced laser-based fluorescence microstructure profiler (TurboMAP-L) for measuring bio-physical coupling in aquatic systems', *Journal of Plankton Research*, 31: 1441-52.

Doubell, Mark J., Jennifer C. Prairie, and Hidekatsu Yamazaki. 2014. 'Millimeter scale profiles of chlorophyll fluorescence: Deciphering the microscale spatial structure of phytoplankton', *Deep-Sea Research Part II: Topical Studies in Oceanography*, 101: 207-15.

Drost, Edwin J. F., Ryan J. Lowe, Greg N. Ivey, and Nicole L. Jones. 2018. "Wave-Current Interactions in the Continental Shelf Bottom Boundary Layer of the Australian North West Shelf During Tropical Cyclone Conditions." *Continental Shelf Research* 165: 78-92.

Dyer, K. R. 1989. 'Sediment processes in estuaries: Future research requirements', *Journal of Geophysical Research*, 94: 14327-39.

Dyer, K. R., and A. J. Manning. 1999. 'Observation of the size, settling velocity and effective density of flocs, and their fractal dimensions', *Journal of Sea Research*, 41: 87-95.

Eaton, J.K., and J.R. Fessler. 1994. 'PREFERENTIAL CONCENTRATION OF PARTICLES BY TURBULENCE', *International Journal of Multiphase Flow*, 20: 169-209.

Engel, Anja. 2000. 'The role of transparent exopolymer particles (TEP) in the increase in apparent particle stickiness (α) during the decline of a diatom bloom', *Journal of Plankton Research*, 22: 485-97.

Falkowski, Paul G., and Matthew J. Oliver. 2007. 'Mix and match: how climate selects phytoplankton', *Nature Reviews Microbiology*, 5: 813-19.

Fettweis, Michael, Matthias Baeye, Dimitry Van der Zande, Dries Van den Eynde, and Byung Joon Lee. 2014. 'Seasonality of floc strength in the southern North Sea', *Journal of Geophysical Research: Oceans*, 119: 1911-26.
Fofonoff, N, P., and R. C MIllard Jr. 1983. 'Algorithms for cumputation of fundamental properites of seawater', *UNESCO technical papers in marine science*, 44.

Foloni-Neto, Herminio, Rolf Lueck, Yoshiro Mabuchi, Hisato Nakamura, Masakazu Arima, and Hidekatsu Yamazaki. 2014. 'A new quasi-horizontal glider to measure biophysical microstructure', *Journal of Atmospheric and Oceanic Technology*, 31: 2278-93.

Franks, P. J. S., and J. S. Jaffe. 2001. 'Microscale distributions of phytoplankton: Initial results from a two-dimensional imaging fluorometer, OSST', *Marine Ecology Progress Series*, 220: 59-72.

Gallager, Scott M., Hidekatsu Yamazaki, and Cabell S. Davis. 2004. 'Contribution of fine-scale vertical structure and swimming behavior to formation of plankton layers on Georges Bank', *Marine Ecology Progress Series*, 267: 27-43.

Gehlen, M., L. Bopp, N. Emprin, O. Aumont, C. Heinze, and O. Ragueneau. 2006. 'Reconciling surface ocean productivity, export fluxes and sediment composition in a global biogeochemical ocean model', *Biogeosciences*, 3: 521–37.

Geyer, W. Rockwell, Malcolm E. Scully, and David K. Ralston. 2008. 'Quantifying vertical mixing in estuaries', *Environmental Fluid Mechanics*, 8: 495-509.
Goda, Yoshimi, and Masanobu Kudaka. 2007. 'On the role of spectral width and shape parameters in control of indiviual wave height distribution', *Coastal Engineering Journal*, 49: 311-35.

Graham, Goerge, and A. M. Nimmo Smith. 2010. 'The application of holography to the analysis of size and settling velocity of suspended cohesive sediments', *Limnology and Oceanography: Methods*, 8: 1-15.

Gurvich, A.S., and A.M. Yaglom. 1993. 'Breakdown of Eddies and Probability Distributions for Small-Scale Turbulence', *Physics of Fluids*, 10: 59-65.

Guseva, Ksenia, and Ulrike Feudel. 2017. 'Aggregation and fragmentation dynamics in random flows: From tracers to inertial aggregates.', *Physical Review E*, 95.

Hill, Paul S., George Voulgaris, and John H. Trowbridge. 2001. 'Controls on floc size in a continental shelf bottom boundary layer', *Journal of Geophysical Research*, 106: 9543-43.

Irwin, A. J., Z. V. Finkel, F. E. Muller-Karger, and L. Troccoli Ghinaglia. 2015. 'Phytoplankton adapt to changing ocean environments', *Proc Natl Acad Sci U S A*, 112: 5762-6.

Jackson, George A. 1990. 'A model of the formation of marine algal flocs by physical coagulation processes', *Deep Sea Research Part A, Oceanographic Research Papers*, 37: 1197-211.

Jackson, George A., David M. Checkley, and Michael Dagg. 2015. 'Settling of particles in the upper 100 m of the ocean detected with autonomous profiling floats off California', *Deep Sea Research Part I: Oceanographic Research Papers*, 99: 75-86.

Jouandet, M. P., G. A. Jackson, F. Carlotti, M. Picheral, L. Stemmann, and S. Blain. 2014. 'Rapid formation of large aggregates during the spring bloom of Kerguelen Island: Observations and model comparisons', *Biogeosciences*, 11: 4393-406.

Khelifa, Ali, and Paul S. Hill. "Models for Effective Density and Settling Velocity of Flocs Models for Effective Density and Settling Velocity of Flocs Models Pour La Densité Effective Et La Vitesse De Sédimentation De Flocs." *Journal of Hydraulic Research* 44, no. 3 (2017): 309-401.

Kiørboe, Thomas, K. P. Andersen, and H. G. Dam. 1990. 'Coagulation efficiency and aggregate formation in marine phytoplankton', *Marine Biology*, 107: 235-45.
Kiørboe, Thomas. 2000. 'Colonization of marine snow aggregates by invertebrate zooplankton: Abundance, scaling, and possible role', *Limnology and Oceanography*, 45: 479-84.

Kiørboe, Thomas. 2001. 'Formation and fate of marine snow: small-scale processes with large- scale implications', *Scientia Marina*, 65: 57-71.
Kiøboe, T. 2001. 'Formation and fate of marine snow: small-scale processes with large-scale implications', *Scientia Marina*, 65: 57-71.

Kiørboe, T. 2003. 'Marine snow microbial communities: scaling of abundances with aggregate size', *Aquatic Microbial Ecology*, 33: 67-75.

Kiorboe, T., K. Tang, H. P. Grossart, and H. Ploug. 2003. 'Dynamics of microbial communities on marine snow aggregates: colonization, growth, detachment, and grazing mortality of attached bacteria', *Appl Environ Microbiol*, 69: 3036-47.

Kokubu, Yusaku, Hidekatsu Yamazaki, Takeyoshi Nagai, and Edward S. Gross. 2013. 'Mixing observations at a constricted channel of a semi-closed estuary: Tokyo Bay', *Continental Shelf Research*, 69: 1-16.

Kolmogorov, A. N. 1941 b. 'On the logarithmical normal particle size distribution caused by particle crushing', *Doklady Akademii Nauk SSSR*, 31: 99-102.

Larsen, Laurel G., Judson W. Harvey, and John P. Crimaldi. 2009. 'Morphologic and transport properties of natural organic floc', *Water Resources Research*, 45: 1-13.

Larson, E., and Alan L. Shanks. 1996. 'Consumption of marine snow by two species of juvenile mullet and its contribution to their growth', *Marine Ecology Progress Series*, 130: 19-28.

Larson, E., and Alan L. Shanks. 1996. 'Consumption of marine snow by two species of juvenile mullet and its contribution to their growth', *Marine Ecology Progress Series*, 130: 19-28.

Laurenceau-Cornec, E. C., T. W. Trull, D. M. Davies, S. G. Bray, J. Doran, F. Planchon, F. Carlotti, M. P. Jouandet, A. J. Cavagna, A. M. Waite, and S. Blain. 2015. 'The relative importance of phytoplankton aggregates and zooplankton fecal pellets to carbon export: Insights from free-drifting sediment trap deployments in naturally iron-fertilised waters near the Kerguelen Plateau', *Biogeosciences*, 12: 1007-27.

Li, Xiao-Yan, Jian-Jun Zhang, and Joseph H. W. Lee. 2004. 'Modelling particle size distribution dynamics in marine waters', *Water Research*, 38: 1305-17.

Lueck, Rolf G., Fabian Wolk, and Hidekatsu Yamazaki. 2002. 'Oceanic Velocity Microstructure Measurements in the 20th Century', *Journal of Oceanography*, 58: 153-74.

Mari, Xavier, Jean-Pascal Torréton, Claire Bich-Thuy Trinh, Thierry Bouvier, Chu Van Thuoc, Jean-Pierre Lefebvre, and Sylvain Ouillon. 2012. 'Aggregation dynamics along a salinity gradient in the Bach Dang estuary, North Vietnam', *Estuarine, Coastal and Shelf Science*, 96: 151-58.

Mari, Xavier, Uta Passow, Christophe Migon, Adrian B. Burd, and Louis Legendre. 2017. 'Transparent exopolymer particles: Effects on carbon cycling in the ocean', *Progress in Oceanography*, 151: 13-37.

McCave, I. N. 1984. 'Size spectra and aggregation of suspended particles in the deep ocean', *Deep Sea Research Part A. Oceanographic Research Papers*, 31: 329-52.

Mikkelsen, Ole A., Paul S. Hill, and Timothy G. Milligan. 2006. 'Single-grain, microfloc and macrofloc volume variations observed with a LISST-100 and a digital floc camera', *Journal of Sea Research*, 55: 87-102.

Najdek, M., M. Blažina, D. Fuks, I. Ivančić, and T. Šilović. 2011. 'Intrusion of high-salinity water causes accumulation of transparent exopolymer particles (TEP) in the northern Adriatic Sea', *Aquatic Microbial Ecology*, 63: 69-74.

Nasmyth, P. 1970. 'Oceanic Turbulence', *Ph.D. Thesis, University of British Columbia*: 69.

Oakey, N. S., and J. A. Elliott. 1982. 'Dissipation Within the Surface Mixed Layer', *Journal of Physical Oceanography*, 12: 171-85.
Organic Matter in Waters Adjacent to Japan', *journal of the Oceanographical Society of Japan*, 8: 113-26.

Owen, Robert B., and Alex a Zozulya. 2000. 'In-line digital holographic sensor for monitoring and characterizing marine particulates', *Optical Engineering*, 39: 2187-87.

Passow, U. 2002. 'Production of transparent exopolymer particles (TEP) by phyto- and bacterioplankton', *Marine Ecology Progress Series*, 236: 1-12.

Passow, U., and C. A. Carlson. 2012. 'The biological pump in a high CO_2 world', *Marine Ecology Progress Series*, 470: 249-71.

Petrik, Colleen M., George A. Jackson, and David M. Checkley. 2013. 'Aggregates and their distributions determined from LOPC observations made using an

autonomous profiling float', *Deep Sea Research Part I: Oceanographic Research Papers*, 74: 64-81.

Prairie, J. C., K. Ziervogel, C. Arnosti, R. Camassa, C. Falcon, S. Khatri, R. M. McLaughlin, B. L. White, and S. Yu. 2013. 'Delayed settling of marine snow at sharp density transitions driven by fluid entrainment and diffusion-limited retention', *Marine Ecology Progress Series*, 487: 185-200.

Ruiz, J., and Alfredo Izquierdo. 1997. 'A simple madel for the break-up of marine aggregates by turbulent shear', *Oceanographica Acta*, 20: 597-605.
Ruiz, J., D. Macias, and Francesc Peters. 2004. 'Turbulence increases the average settling velocity of phytoplankton cells', *PNAS*, 101: 17720-24.

Safak, I., M. A. Allison, and A. Sheremet. 2013. 'Floc variability under changing turbulent stresses and sediment availability on a wave energetic muddy shelf', *Continental Shelf Research*, 53: 1-10.

Shanks, Alan L., and Jonathan D. Trent. 1979. 'Marine Snow: Microscale nutrient patches 1', *Limnology and Oceanography*, 24: 850-54.

Shanks, Alan L. 2002. 'The abundance, vertical flux, and still-water and apparent sinking rates of marine snow in a shallow coastal water column', *Continental Shelf Research*, 22: 2045-64.

Silver, Mary, and Alan L. Shanks. 1978. 'Marine Snow: Microplankton Habitat and Source of Small-Scale Patchiness in Pelagic Populations', *Science*, 201: 371-73.

Simon, Meinhard, Hans Peter Grossart, Bernd Schweitzer, and Helle Ploug. 2002. 'Microbial ecology of organic aggregates in aquatic ecosystems', *Aquatic Microbial Ecology*, 28: 175-211.

Smyth, W. D., and J. N. Moum. 2019. '3D Turbulence.' in H. Bokuniewicz, P. Yger and J. Kirk Cochran (eds.), *Encyclopedia of Ocean Sciences* (Academic Press).

Sogawa, Sayaka, Kiyotaka Hidaka, Yasuhiro Kamimura, Masanori Takahashi, Hiroaki Saito, Yuji Okazaki, Yugo Shimizu, and Takashi Setou. "Environmental Characteristics of Spawning and Nursery Grounds of Japanese Sardine and Mackerels in the Kuroshio and Kuroshio Extension Area." *Fisheries Oceanography* 28, no. 4 (2019): 454-67.

Soos, M., A. S. Moussa, L. Ehrl, J. Sefcik, H. Wu, and M. Morbidelli. 2008. 'Effect of shear rate on aggregate size and morphology investigated under turbulent conditions in stirred tank', *Journal of Colloid And Interface Science*, 319: 577-89.

Soulsby RL (1995) Bed shear-stresses due to combined waves and currents. In: Advances in coastal morphodynamics 4 Delft Hydraulics Delft, 4-23

Squires, Kyle D., and John K. Eaton. 1991. 'Preferential concentration of particles by turbulence', *Physics of Fluids A: Fluid Dynamics*, 3: 1169-78.

Stemmann, Lars, George A. Jackson, and Debby Ianson. 2004. 'A vertical model of particle size distributions and fluxes in the midwater column that includes biological and physical processes—Part I: model formulation', *Deep Sea Research Part I: Oceanographic Research Papers*, 51: 865-84.

Stocker, R. 2002. 'Marine Microbes See a Sea of Gradients', *Science*, 338: 628-33.

Swart DH (1974) Offshore sediment transport and equilibrium beach profiles. Delft Hydraul. Lab. Publ. No. 131.

Tennekes, H., and John Lumley. 1972. *A First Course in Turbulence* (The MIT Press).

Tsujita, Tomiki. 1953. 'A Preliminary Study on Naturally Occurring Suspended

Turner, Jefferson T. 2015. 'Zooplankton fecal pellets, marine snow, phytodetritus and the ocean's biological pump', *Progress in Oceanography*, 130: 205-48.

Wiberg, Patricia L., and Christopher R. Sherwood. "Calculating Wave-Generated Bottom Orbital Velocities from Surface-Wave Parameters." *Computers & Geosciences* 34, no. 10 (2008): 1243-62.

Winterwerp, Johan C. 1998. 'A simple model for turbulence induced flocculation of cohesive sediment', *Journal of Hydraulic Research*, 36: 309-26.

Winterwerp, J. C. 2002. 'On the flocculation and settling velocity of estuarine mud', *Continental Shelf Research*, 22: 1339-60.

Wolk, Fabian, Laurent Seuront, and Hidekatsu Yamazaki. "Spatial Resolution of a New Micro-Optical Probe for Chlorophyll and Turbidity." *Journal of Tokyo University of Fisheries* 87 (2001): 13-21.

Yamazaki, H., and T. Osborn. 1990. 'Dissipation Estimates for Stratified Turbulence', *Journal of Geophysical Research*, 95: 9739-44.

Yamazaki, Hidekatsu, and Kyle Squires. 2003. 'An Application of the Lognormal Theory to Moderate Reynolds Number Turbulent Structures.' in (CRC Press).